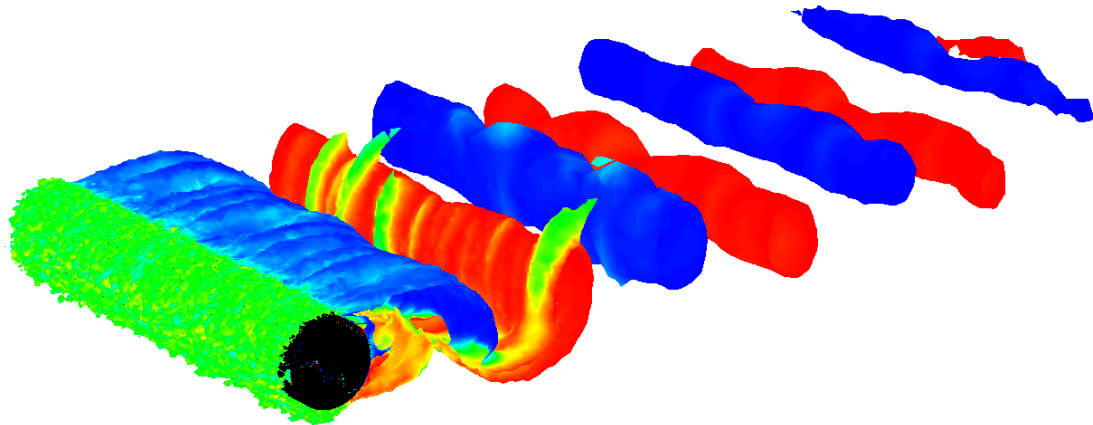




CHALMERS
UNIVERSITY OF TECHNOLOGY



CFD simulation of hydrodynamic loads on a floating vertical axis wind turbine

Master's thesis in Innovative and Sustainable Chemical Engineering

MARCUS BUDESINSKY

MASTER'S THESIS 2019

**CFD simulation of hydrodynamic loads on a
floating vertical axis wind turbine**

MARCUS BUDESINSKY



CHALMERS
UNIVERSITY OF TECHNOLOGY

Department of Chemistry and Chemical Engineering
CHALMERS UNIVERSITY OF TECHNOLOGY
Gothenburg, Sweden 2019

CFD simulation of hydrodynamic loads on a floating vertical axis wind turbine
MARCUS BUDESINSKY

© MARCUS BUDESINSKY, 2019.

Supervisor: Daniel Grönberg, Alten AB
Examiner: Ronnie Andersson, Department of Chemistry and Chemical Engineering

Master's Thesis 2019
Department of Chemistry and Chemical Engineering

Chalmers University of Technology
SE-412 96 Gothenburg
Telephone +46 31 772 1000

Cover: Vortex shedding behind a rotating cylinder.

Typeset in L^AT_EX
Gothenburg, Sweden 2019

CFD simulation of hydrodynamic loads on a floating vertical axis wind turbine
MARCUS BUDESINSKY
Department of Chemistry and Chemical Engineering
Chalmers University of Technology

Abstract

Offshore wind is a promising alternative for renewable energy generation. Wind velocities are generally higher at sea and there is a large availability of sea area. The increased construction costs at large depths motivates the usage of floating wind turbines. SeaTwirl are developing the floating vertical axis wind turbine SeaTwirl S2. The underwater structure of the turbine rotates with the rest of the wind turbine, generating a lift force from the passing currents by the Magnus effect. This thesis presents the development of a CFD model for estimation of the magnitude of the hydrodynamic forces (lift, drag), and friction losses. 2D and 3D models for simulations of rotating cylinders were developed and validated with published data. Simulations were done using a SST $k-\omega$ turbulence model in ANSYS Fluent. Both models were run in the speed ratio range of $\alpha = 0-14$ at a Reynolds number of $5 \cdot 10^6$. It was found that both models yielded lift coefficient results in line with experimental data in the speed ratio range of $0 \leq \alpha \leq 6$. At higher speed ratios the lift force was overestimated for the 2D model, and underestimated by the 3D model. Differences between the 2D and 3D models were attributed to the formation of 3D instabilities which reduced lift and increased drag. The results from the cylinder simulations were used to develop a 3D model for simulations of the spar type floating element under typical operating conditions. Operational forces amounting to 71kN lift and 21 kN drag, with friction losses of kW were observed. The primary conclusion is that the lift force and friction moment are captured well with the CFD models, while the drag force estimation is uncertain.

Keywords: Computational fluid dynamics, CFD, Magnus effect, rotating cylinder, vertical axis wind turbine, vortex shedding.

Acknowledgements

I would like to thank my supervisors Daniel Grönberg, Niklas Persson and Umut Cirik at Alten Sverige for continuous support and feedback on my work. Thanks to Erik Östermark at Alten for technical support and lunch company. I would also like to thank Jonas Boström at SeaTwirl AB for input on the project and for providing technical data. Lastly, thanks to Associate Professor Ronnie Andersson for taking the time to be my examiner.

Marcus Budesinsky, Gothenburg, May 2019

Contents

List of Symbols	x
1 Introduction	1
1.1 The future of wind power	1
1.2 Vertical axis wind turbines	2
1.3 SeaTwirl S2	2
1.4 Literature review	3
1.4.1 Experimental studies	4
1.4.2 Numerical studies	5
1.5 Problem statement	6
1.6 Demarcations	6
1.7 Method	6
2 Theory	7
2.1 Governing equations	7
2.2 Turbulence	8
2.2.1 Reynolds-averaged Navier-Stokes	8
2.2.2 Turbulence modeling	9
2.2.3 The standard $k-\epsilon$ model	9
2.2.4 The $k-\omega$ model	10
2.2.5 The SST $k-\omega$ model	11
2.2.6 Curvature correction	12
2.2.7 Wall treatment	12
2.2.8 Wall roughness effects	14
2.3 Hydrodynamic loads on rotating cylinders	14
2.3.1 Estimation of forces	15
3 Methods	17
3.1 Domain	17
3.1.1 2D cylinder simulations	17
3.1.2 3D cylinder simulations	18
3.1.3 3D spar simulations	19
3.2 Mesh	20
3.2.1 2D mesh	20
3.2.2 3D mesh	21
3.2.3 Spar mesh	22

3.3	Simulation settings	23
3.4	Boundary conditions	24
3.5	Forces and moments	24
3.6	Ocean current velocity profile	25
4	Results and discussion	26
4.1	2D simulations	26
4.1.1	Domain size	26
4.1.2	Mesh independence	27
4.1.3	Inlet turbulence intensity	28
4.1.4	Comparison with reference case	29
4.1.5	Transient flow behaviour	30
4.1.6	Surface roughness effects	33
4.2	3D cylinder simulations	34
4.3	Model evaluation	37
4.4	Spar simulation	39
4.4.1	Simulations with constant velocity	39
4.4.2	Simulations in operating conditions	39
4.5	Comparison of force estimations	44
5	Conclusion	45
6	Recommendations for further work	46
	References	47
A	Appendix: Surface roughness effects	I
B	Appendix: Potential flow theory	II
C	Appendix: Summary of experimental data	III
D	Appendix: 3D aspect ratio effects	V
E	Appendix: 2D vortex shedding data	VI

List of Symbols

Latin Symbols

A	Area	m^2
C_D	Drag coefficient	-
C_f	Skin friction coefficient	-
C_L	Lift coefficient	-
C_M	Moment coefficient	-
D	Diameter	m
F_D	Drag force	N
F_L	Lift force	N
k	Turbulent kinetic energy	m^2/s^2
K^+	Dimensionless roughness constant	-
M_f	Friction moment	$\text{N} \cdot \text{m}$
P	Pressure	Pa
r	Radius	m
Re	Reynolds number	-
u	Velocity	m/s
u_*	Wall friction velocity	m/s
U_∞	Free-stream velocity	m/s
y^+	Dimensionless wall distance	-

Greek symbols

α	Velocity ratio	-
δ_{ij}	Kronecker delta	-
κ	Von Kármán constant	-
μ	Fluid dynamic viscosity	$\text{Pa} \cdot \text{s}$
μ_t	Turbulent dynamic viscosity	$\text{Pa} \cdot \text{s}$
ν	Fluid kinematic viscosity	m^2/s
ν_t	Turbulent viscosity	m^2/s
ω	Angular velocity	$1/\text{s}$
ω	Specific turbulence dissipation rate	$1/\text{s}$
ρ	Fluid density	kg/m^3
τ_w	Wall shear stress	Pa
ε	Turbulent energy dissipation rate	m^2/s^3
$\vec{\omega}$	Vorticity	$1/\text{s}$

1

Introduction

1.1 The future of wind power

Global warming, climate change, air pollution and the future insecurity of fossil fuel supply are some of the major driving forces for a transition to renewable energy generation. The European union has set long-term goals to achieve net-zero greenhouse gas emissions by 2050. Key milestones in this effort is the target to reach an energy consumption from renewable resources totaling 20 % by 2020 and 27 % by 2030. [1] One of the most promising alternatives for large scale renewable energy generation is wind power. The utilization of wind energy for electricity production dates back to the 1880:s, when the first small experimental turbines were developed. During the early 20th century wind turbines were mainly used in the USA for small-scale electricity generation in rural areas not connected to the grid. With the widespread electrification in the 1930:s and the drop in fuel prices after the second world war, wind power was on the decline. However, this changed with the fuel crisis in the 70:s, which saw the start of the development of large scale wind turbines. [2] In more recent years wind power has developed rapidly, with a capacity covering 14 % of the EU:s energy demand in 2018. [3]

EU predicts that by 2050 a large share of renewable power generation will be provided by off-shore wind power. [1] The advantages of siting wind power offshore are the vast availability of sea area and higher wind speeds at open sea, potentially increasing the power generated compared to wind turbines located on land. Furthermore, offshore wind turbines located far away from the coast have low restrictions on visual impact and noise. Drawbacks are associated with increased construction and maintenance costs. Wind turbines are traditionally fixed to the seafloor by a foundation, and the cost of constructing the foundation increases with the water depth. An alternative is floating wind turbines moored to the seafloor. This allows siting of wind turbines in deep water where a fixed foundation would not be economically feasible. [4] The dynamic behaviour of floating wind turbines is however affected by the ocean current and waves.

1.2 Vertical axis wind turbines

Wind turbines are generally classified according to the axis of rotation into horizontal axis wind turbines (HAWT:s) and vertical axis wind turbines (VAWT:s). Both variants work on the principle of converting the kinetic energy of the wind to electricity through mechanical work. The rotors on either variant utilizes aerodynamic lift and/or drag to capture the energy of the wind, which is converted to electricity by turning a generator.

A comparison of the two types show that the vertical axis wind turbines have an overall simpler design and feature a number of advantages as well as disadvantages compared to HAWT:s. The vertical axis of rotation allows mechanical and power generating equipment to be placed close to the ground, which can reduce maintenance costs as well as increase the safety for maintenance personnel. VAWT:s function independent of wind direction and therefore does not need a costly yaw control system, which is needed for HAWT:s to face the wind direction. Disadvantages with VAWT:s includes the lack of ability to self-start which means that VAWT:s typically require a starter motor. Furthermore, VAWT:s have a lower wind energy conversion efficiency compared to HAWT:s. [2].

1.3 SeaTwirl S2

SeaTwirl S2 is a floating vertical axis wind turbine under development. A schematic description of the wind turbine is shown in Figure 1.1. The wind turbine consists of a rotor with airfoils mounted on a tower. The tower is connected to a sub-sea structure, consisting of a spar type floating element and a keel. The weight of the wind turbine is carried by the buoyancy of the floating element, and the keel increases vertical stability by providing a low center of gravity. The rotor, tower and underwater structure rotates as one piece. Electricity is generated by a generator located close to the water surface. The low location of the generator makes it easily accessible for maintenance. The generator does not rotate and is anchored to the seabed by mooring lines. [5]

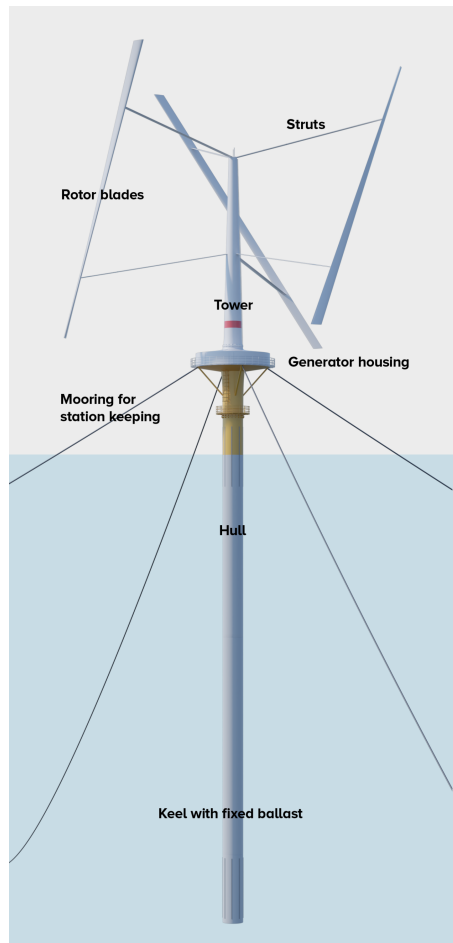


Figure 1.1: Concept for the SeaTwirl S2 wind turbine.

Due to the water currents and rotation of the spar, the underwater structure will be subject to hydrodynamic forces in the form of lift (as a result of the Magnus effect) and drag. The spar is also subject to a friction torque as the rotation causes friction with the surrounding water. Assessment of the forces and moments are of great importance in the design process of the wind turbine. It is therefore of interest to develop a computational method that can predict the magnitude of the hydrodynamic forces.

1.4 Literature review

This section aims to give a review of the publicly available literature covering experiments and numerical simulations of flow past rotating cylinders. The main focus is summarizing literature concerning high Reynolds number flows at high speed ratios, but important works concerning other flow regimes are also included. Table 1.1 presents a summary of important experimental and numerical studies. Figure C.1 in Appendix C shows a summary of the reported experimental lift coefficients.

Table 1.1: Overview of important experimental and numerical studies.

Experimental studies				
Year	Author	Re	α	Comment
1923	Reid [6]	$5.6 \cdot 10^4$	0-4.3	-
1925	Prandtl [7]	-	0-3.4	-
1934	Thom [8]	$4.5-47.5 \cdot 10^3$	0-6.5	With endplates
1944	Theodorsen [9]	$0-7 \cdot 10^6$	-	Friction moment
1993	Tokumar & Dimotakis [10]	$3.8 \cdot 10^3$	0-10	-
2012	Carstensen [11]	$1 \cdot 10^4 - 6 \cdot 10^4$	0-6	DeepWind turbine
Numerical studies				
Year	Author	Re	α	Comment
2002	Mittal & Kumar [12]	200	0-5	2D, laminar
2003	Stojković [13]	60-200	0-6	2D, laminar
2004	Mittal [14]	200	5	3D, laminar
2010	Karabelas et al. [15]	140,000	0-2	3D, LES
2011	Vita [16]	$5 \cdot 10^6$	1.4-5.2	2D, SST $k-\omega$
2011	Karabelas et al. [17]	$5 \cdot 10^5 - 5 \cdot 10^6$	2-8	2D, RANS

1.4.1 Experimental studies

Rotating cylinders in cross flow has been of interest since the early 1920s and have been investigated in many studies. Early studies include those of Prandtl [7] who predicted a theoretical maximum coefficient of lift of $C_{L,Max} = 4\pi$. Reid [6] investigated rotating cylinders in air, and found that the lift force increased steadily with an increasing rotational speed, with values of C_L surpassing the upper limit proposed by Prandtl. It was also found that the introduction of a circulating flow significantly decreased drag compared to a stationary cylinder, although the drag decrease was less significant at high speed ratios.

Theodorsen [9] investigated the drag on fast spinning cylinders in high Reynolds numbers flows, and developed empirical expressions for the estimation of the drag and friction torque as a function of the Reynolds number based on the rotational velocity.

Tokumar and Dimotakis [10] conducted experimental studies of the lift force on a rotating cylinder at $Re=3.8 \cdot 10^3$ for speed ratios 0 to 10. It was found that the lift increased with an increasing speed ratio, with no apparent maximum value. Vortex shedding was observed for $\alpha < 2.5$, and ceased for higher speed ratios. By introducing forced oscillations, the wake could be stabilized with an increase in lift as a result. An important conclusion was that the lift coefficient is dependant on the aspect ratio (ratio of length to diameter) of the cylinder, with larger aspect ratios yielding larger maximum lift coefficients.

Carstensen et al. [11] conducted experimental studies on a rough rotating cylinder in

water for the floating wind turbine DeepWind. Tests were done with current speeds in the range of $U=0.06-0.7$ m/s with a Reynolds number in the range of $Re=10^4-10^5$. The corresponding speed ratio was in the range of $\alpha=0-6.15$. No information about the flow stability and vortex shedding was reported. The observed drag coefficient is similar to results from Reid [6] for low speed ratios, although an increasing drag is observed for higher speed ratios. The measured lift coefficient is slightly higher than results from Tokumaru [10] at high speed ratios.

1.4.2 Numerical studies

Numerical simulations of flows past rotating cylinders are numerous, but are mostly confined to laminar flows or low Reynolds number turbulent flows at speed ratios $\alpha \leq 10$. For high Reynolds number flows only a handful of articles are available. For laminar flows Mittal and Kumar [12] performed extensive numerical simulations at $Re=200$, with an α ranging from 0 to 5. It was found that the behaviour of vortex shedding was highly dependant on α , with a Von Kármán street observed in the cylinder wake for speed ratios in the the range $0 \leq \alpha \leq 1.9$. For higher speed ratios the flow alternated between steady and unsteady states, depending on the speed ratio.

Mittal et. al. also performed 3D simulations for $Re=200$ and $\alpha=5$ [14]. It was found that the aspect ratio of the cylinder had a large effect on the magnitude on the lift force, with a decrease in lift and an increase in drag for low aspect ratios. Furthermore, 3D-instabilities caused the flow to become unstable although a purely two-dimensional flow has been reported stable for $\alpha=5$ [12]. This caused a decrease in lift and an increase in drag compared to a 2D case.

Few numerical studies have been done on rotating cylinders with high velocity ratios and Reynolds numbers, which is the regime in which the SeaTwirl wind turbine operates. Available literature include the work of Karabelas who conducted studies on a spinning cylinder using LES at $Re=1.4 \cdot 10^5$ [15]. Karabelas concluded that the lift coefficient increased almost linearly with the speed ratio in the examined interval of $0 \leq \alpha \leq 2$, while the drag coefficient decreased. The flow was found to display vortex shedding for low speed ratios, and becoming stable for $\alpha \geq 1.5$.

Karabelas also conducted a numerical simulation using a modified $k-\varepsilon$ model at Reynolds numbers ranging from $5 \cdot 10^5$ to $5 \cdot 10^6$ [17] and $\alpha = 0$ to $\alpha = 8$. As steady simulations were ran no characteristics of vortex shedding was presented. The mean flow was found to reach steady state for all the examined cases. The computational model correlated well with experimental data at low speed ratios ($\alpha=0-1$).

The only published study on the hydrodynamics of a rotating vertical axis wind turbine are by Vita [16], who conducted 2D simulations using an in-house RANS/URANS CFD solver. Vita used a SST $k-\omega$ turbulence model and examined speed ratios ranging from 1.4 to 5.2 with a Reynolds number of $5 \cdot 10^6$. Vita found vor-

tex shedding at $\alpha=1.4$, and a steady wake for the other examined cases. Vita's simulations showed a good agreement with experimental data, with a slight underestimation of the lift force at the highest speed ratio. Furthermore, data for the drag and friction moments was presented.

1.5 Problem statement

The aim of this thesis is to develop a CFD simulation method to estimate the hydrodynamic forces on the rotating submerged spar of a floating vertical axis wind turbine. The main investigated parameters are lift due to the Magnus effect, drag and torque due to friction. In short, the main objectives are:

- Simulate the flow behaviour around a rotating cylinder using a 2D CFD computational model.
- Evaluate the model sensitivity regarding mesh resolution, turbulence models and boundary conditions. Evaluate the accuracy of the model by comparing the results with experimental data available from literature.
- Develop a 3D model for a cylinder and compare the results with those from the 2D model.
- Develop a 3D simulation model for the spar.

1.6 Demarcations

The CFD model will be limited to simulations of steady currents, and without any form of wave modeling. The spar will be modeled as steady without any moment induced by the hydrodynamic loads. The simulation will only use steady rotational speeds, and will not be coupled to any aerodynamic loads from the wind turbine tower and blades. The cylinder surface is assumed to be smooth, and the effects of marine growth will not be considered.

1.7 Method

This Master's thesis was performed at Alten Sverige AB in Gothenburg. The main parts of this study were a literature survey and model development. Modelling of the wind turbine was done using the commercial CFD software ANSYS Fluent. A more thorough description of the simulation method is given in Chapter 3.

2

Theory

This chapter presents the theoretical background to the computational methods used in this study. Governing equations for fluid flow are presented initially, followed by a section on turbulence and turbulence modelling. The last section addresses flow around rotating cylinders.

2.1 Governing equations

The governing equations for fluid flow originates from conservation laws for mass and momentum. The transport equations are presented based on the Eulerian representation where the flow field is a function of space and time. Mass conservation is given by the continuity equation:

$$\frac{\partial \rho}{\partial t} + \frac{\partial \rho u_j}{\partial x_j} = 0 \quad (2.1)$$

For incompressible flow the change in density with time is zero and the equation reduces to:

$$\frac{\partial u_j}{\partial x_j} = 0 \quad (2.2)$$

The conservation of momentum is given by the Navier-Stokes equation of motion (no body force):

$$\frac{\partial u_i}{\partial t} + u_j \frac{\partial u_i}{\partial x_j} = -\frac{1}{\rho} \frac{\partial p}{\partial x_i} + \nu \frac{\partial^2 u_i}{\partial x_j \partial x_j} \quad (2.3)$$

2.2 Turbulence

Turbulence occurs in most common fluid flows ranging from flows in engineering applications to flows occurring in nature, and is of significant importance in the study of these types of systems. There is no unanimous definition of turbulence, although turbulence is often characterized based on features of the fluid flow. Turbulent flows are highly irregular and chaotic. Turbulence generally arises from instabilities in the flow occurring when the inertial forces are much larger than the dampening viscous forces. The chaotic motion of the fluid greatly enhances the transport of species, heat and momentum. Turbulence is also dissipative, meaning that there is a transport of turbulent kinetic energy through the turbulent structures (eddies) from the largest scales down to the smallest scales. Energy is extracted from the mean flow by large eddies and cascades to smaller scales by inviscid processes. At the smallest turbulent scales, the Kolmogorov scales, energy is dissipated to heat by viscous forces. Lastly, turbulence is a continuum phenomena as the smallest eddies are considerably larger than the molecular length scales. [18]

2.2.1 Reynolds-averaged Navier-Stokes

The stochastic nature of turbulence combined with the wide range of turbulent length and time scales means that a very high spatial and temporal resolution is needed to solve the Navier-Stokes equations for turbulent flows by direct numerical simulation (DNS). The high computational cost required for DNS makes this option unfeasible for most engineering applications. An alternative is to solve the mean (time averaged) turbulent flow field. This approach greatly reduces the computational cost for solving the flow equations. Using a Reynolds decomposition the instantaneous velocities can be separated into a mean $\langle u_i \rangle$, and a fluctuating part u'_i :

$$u_i = \langle u_i \rangle + u'_i \quad (2.4)$$

Applying time averaging and a Reynolds decomposition for the velocity to the Navier-Stokes equations (2.3), yields the Reynolds-averaged Navier-Stokes (RANS) equations [19]:

$$\frac{\partial \langle u_i \rangle}{\partial x_i} = 0 \quad (2.5)$$

$$\frac{\partial \langle u_i \rangle}{\partial t} + \langle u_i \rangle \frac{\partial \langle u_i \rangle}{\partial x_j} = -\frac{1}{\rho} \frac{\partial \langle P \rangle}{\partial x_i} + \nu \frac{\partial^2 \langle u_i \rangle}{\partial x_j^2} - \frac{\partial \langle u'_i u'_j \rangle}{\partial x_j} \quad (2.6)$$

Compared to the Navier-Stokes equations (2.3) an additional term appears in the momentum equation called the Reynolds stress tensor:

$$-\rho \langle u'_i u'_j \rangle \quad (2.7)$$

The Reynolds stress tensor represents the momentum transport by turbulent fluctuations. The tensor is symmetric and second order, and contains six unknowns which has to be solved for. Deriving transport equations for the Reynolds stresses is one way to close the unknown terms. However, doing so introduces third-order moments which are unknown. In general, transport equations for the n th moment contains terms of the $(n + 1)$ th moment. This is referred to as the closure problem, and closure models have to be introduced to solve Equation 2.6.

2.2.2 Turbulence modeling

A common method to close the Reynolds stress tensor is to use the Boussinesq approximation. The Boussinesq approximation assumes that the Reynolds stresses can be modeled analogous to molecular diffusion using a turbulent (eddy) viscosity term:

$$-\langle u'_i u'_j \rangle = \nu_t \left(\frac{\partial \langle u_i \rangle}{\partial x_j} + \frac{\partial \langle u_j \rangle}{\partial x_i} \right) - \frac{2}{3} \rho k \delta_{ij} \quad (2.8)$$

Where $k = 1/2 \langle u_i u_i \rangle$ is the turbulent kinetic energy. Using the Boussinesq approximation the six unknown terms in the Reynolds stress tensor are reduced to two (k and ν_t). Using two-equation turbulence models, the turbulent viscosity is most commonly given in terms of k and some other turbulent variable. The choice of turbulence variables leads to different two-equations models. Commonly used are the k - ε and k - ω models. [18]

2.2.3 The standard k - ε model

The standard k - ε model developed by Jones and Launder [20] is a two-equation turbulence model consisting of transport equations for the turbulent kinetic energy and for the turbulent energy dissipation rate.

Transport of turbulent kinetic energy:

$$\frac{\partial}{\partial t}(\rho k) + \frac{\partial}{\partial x_j}(\rho k \langle u_j \rangle) = \frac{\partial}{\partial x_j} \left[\left(\mu + \frac{\mu_t}{\sigma_k} \right) \frac{\partial k}{\partial x_j} \right] + P_k - \rho \varepsilon \quad (2.9)$$

Transport of turbulent energy dissipation rate:

$$\frac{\partial}{\partial t}(\rho\varepsilon) + \frac{\partial}{\partial x_j}(\rho\varepsilon\langle u_j \rangle) = \frac{\partial}{\partial x_j} \left[\left(\mu + \frac{\mu_t}{\sigma_\varepsilon} \right) \frac{\partial \varepsilon}{\partial x_j} \right] + \frac{\varepsilon}{k} (C_{\varepsilon 1} P_k - C_{\varepsilon 2} \rho \varepsilon) \quad (2.10)$$

Where P_k represents the production of k by velocity fluctuations [18], and is given by:

$$P_k = -\rho \langle u'_i u'_j \rangle \frac{\partial \langle u_j \rangle}{\partial x_i} \quad (2.11)$$

The turbulent dynamic viscosity is modeled as:

$$\mu_t = C_\mu \frac{k^2}{\varepsilon} \quad (2.12)$$

The closure coefficients in equations 2.9 and 2.10 are summarized in Table 2.1.

Table 2.1: Closure coefficients for the k- ε model.

Constant	C_μ	$C_{\varepsilon 1}$	$C_{\varepsilon 2}$	σ_k	σ_ε
Value	0.09	1.44	1.92	1	1.3

The k- ε model works well for a wide range of flows and is a popular choice for engineering applications. There are, however, cases where flows cannot be accurately captured by the k- ε model. Swirling flows, highly anisotropic flows and low Reynolds number flows are examples of flows that are not accurately modeled [18]. Furthermore, the k- ε model is not valid in the near-wall region and dampening functions must be used in the viscous and buffer sublayer [21].

2.2.4 The k- ω model

The k- ω model is a two-equation turbulence model developed by Wilcox [22], which uses transport equations for turbulent kinetic energy and specific turbulent dissipation rate to model the turbulence.

The turbulent kinetic energy k and specific dissipation rate ω is used to model the turbulent viscosity:

$$\nu_t = \frac{k}{\omega} \quad (2.13)$$

The transport equations are:

Transport of turbulent kinetic energy:

$$\frac{\partial}{\partial t}(\rho k) + \frac{\partial}{\partial x_j}(\rho k \langle u_j \rangle) = \rho \tau_{ij} \frac{\partial \langle u_i \rangle}{\partial x_j} - \beta^* \rho k \omega + \frac{\partial}{\partial x_j} \left[\left(\mu + \sigma^* \frac{\rho k}{\omega} \right) \frac{\partial k}{\partial x_j} \right] \quad (2.14)$$

Transport of specific turbulent dissipation rate:

$$\frac{\partial}{\partial t}(\rho\omega) + \frac{\partial}{\partial x_j}(\rho\omega\langle u_j \rangle) = \alpha \frac{\omega}{k} \rho \tau_{ij} \frac{\partial \langle u_i \rangle}{\partial x_j} - \beta \rho \omega^2 + \frac{\partial}{\partial x_j} \left[\left(\mu + \sigma \frac{\rho k}{\omega} \right) \frac{\partial \omega}{\partial x_j} \right] \quad (2.15)$$

where α , β , β^* , σ and σ^* are closure coefficients with values presented in Table 2.2.

Table 2.2: Closure coefficients for the k- ω model.

Constant	α	β	β^*	σ	σ^*
Value	0.56	0.075	0.09	0.5	0.5

The k- ω model is known to perform well in regions with adverse pressure gradients and in the viscous sublayer. Compared to the k- ε model, the k- ω model does not need the use of wall functions in the viscous sublayer. The model does however not perform as well as the k- ε model in the free-stream as it is highly sensitive to the free-stream turbulence variables [21].

2.2.5 The SST k- ω model

The shear stress transport (SST) k- ω model was developed by Menter [21] and is a zonal model that utilizes different sub-models in different parts of the turbulent sublayers. The SST model applies the k- ω model in the near wall region and switches to the k- ε model, using a k- ω formulation, in the free stream. Thus the model builds on the strengths of the two respective models. The transport equation for turbulent kinetic energy is the same as for the k- ω model, given by Equation 2.16:

$$\frac{\partial}{\partial t}(\rho k) + \frac{\partial}{\partial x_j}(\rho k \langle u_j \rangle) = \rho \tau_{ij} \frac{\partial \langle u_i \rangle}{\partial x_j} - \beta^* \rho k \omega + \frac{\partial}{\partial x_j} \left[\left(\mu + \sigma^* \frac{\rho k}{\omega} \right) \frac{\partial k}{\partial x_j} \right] \quad (2.16)$$

The transport of specific turbulent dissipation rate is given by:

$$\begin{aligned} \frac{\partial}{\partial t}(\rho\omega) + \frac{\partial}{\partial x_j}(\rho\omega\langle u_j \rangle) = & \gamma \frac{\omega}{k} \rho \tau_{ij} \frac{\partial \langle u_i \rangle}{\partial x_j} - \beta \rho \omega^2 + \frac{\partial}{\partial x_j} \left[\left(\mu + \sigma \frac{\rho k}{\omega} \right) \frac{\partial \omega}{\partial x_j} \right] \\ & + 2\rho(1 - F_1)\sigma_{\omega 2} \frac{1}{\omega} \frac{\partial k}{\partial x_j} \frac{\partial \omega}{\partial x_j} \end{aligned} \quad (2.17)$$

The blending function F_1 controls which turbulence model is used, and varies with the distance to the wall. In the near wall region, $F_1=1$, and the original k- ω model is

retained. In the free-stream $F_1 = 0$, and the SST model takes the form of a modified k- ε model. Two sets of closure parameters are used, one for the k- ε and one for the k- ω formulation of the model. The parameters are weighted based on the value of F_1 by:

$$\phi = F_1\phi_1 + (1 - F_1)\phi_2 \quad (2.18)$$

where ϕ_1 and ϕ_2 are sets of closure parameters belonging to the k- ε and k- ω models, respectively. [21]

2.2.6 Curvature correction

Eddy viscosity models such as the standard k- ε and SST k- ω model have the limitation of not being able to capture streamline curvature and rotation well. Spalart and Shur [23] proposed a modification to the one equation Spalart-Allmaras turbulence model by introducing a rotation-curvature correction function:

$$f_{rotation} = (1 + c_{r1}) \frac{2r^*}{1 + r^*} [1 - c_{r3} \tan^{-1}(c_{r2}\tilde{r})] - c_{r1} \quad (2.19)$$

Smirnov and Menter [24] modified the function for the SST k- ω turbulence model:

$$f_{r1} = \max(\min(f_{rotation}, 1.25), 0.0) \quad (2.20)$$

where c_{r1} , c_{r2} and c_{r3} in Equation 2.19 are empirical constants set to 1, 2 and 1 respectively. The terms r^* and \tilde{r} are functions of the vorticity and strain rate tensors.

The modified function in Equation 2.20 is multiplied with the production terms in the standard SST k- ω Equations 2.16 and 2.17. The curvature correction term is limited to a lower boundary of 0 for numerical stability and to an upper boundary of 1.25 based on results in [24]. Smirnov and Menter found that the modified function was more accurate than the standard SST k- ω for a number of cases involving streamline curvature and rotation, at only a small increase in computational cost.

2.2.7 Wall treatment

The presence of walls strongly affects the turbulent flow field. At the wall the flow satisfies the no slip condition, meaning that the relative velocity between the fluid and the wall is zero. The flow velocity increases rapidly with an increasing distance from the wall until it reaches the velocity of the free-stream. The large gradients in velocity means that the production of turbulent kinetic energy is largest close to the walls. Therefore it can be important to accurately resolve the near-wall boundary layer for many CFD applications.

The near-wall flow-field is commonly divided into three regions. In the region closest to the wall the viscous forces dominate, effectively dampening the turbulence and causing the flow to be mostly laminar. This layer is known as the viscous sub-layer. In the interim region further away from the wall, the buffer sublayer, the molecular viscosity and turbulence are of equal importance. The outermost layer is called the fully turbulent sub-layer. In this region turbulent forces dominate and viscous forces become negligible. [25]

The dimensionless wall distance y^+ is used to determine the location of a control volume in the boundary layer:

$$y^+ = \frac{yu_*}{\nu} \quad (2.21)$$

where $u_* = \sqrt{\tau_w/\rho}$ is the wall friction velocity and τ_w is the wall shear stress. The location of a cell in the boundary layer is given by [26]:

$0 < y^+ < 5$ Viscous sublayer

$5 < y^+ < 30$ Buffer sublayer

$30 < y^+ < 400$ Fully turbulent sublayer

The k- ω turbulence model is able to resolve the near-wall region down to the viscous sub-layer and should have near wall mesh resolution corresponding to $y^+ = 1$, although values up to $y^+ = 4$ are acceptable. More importantly is that the boundary layer resolution is sufficiently high, with a minimum number of 10, and preferably 20 control volumes in the near-wall boundary layer [25].

For turbulence models that are not valid in the near wall region, such as the k- ϵ model, the viscous and buffer sub-layers are not resolved. Instead, empirical wall functions are employed to bridge the near-wall and the fully turbulent region. These wall functions use the law of the wall to determine the mean velocity in the viscous and buffer sub-layers:

$$U^* = \frac{1}{\kappa} \ln(Ey^*) \quad (2.22)$$

where U^* is the dimensionless velocity, κ is the Von Kármán constant and E is an empirical constant. Turbulent quantities are calculated under the assumption of local equilibrium, which states that the production of turbulent kinetic energy is equal to the dissipation rate closest to the wall. Standard wall functions give good results for a broad range of flows, but fails for flows where the assumptions of constant shear and local equilibrium does not apply, for example when adverse pressure gradients are present. [25]

2.2.8 Wall roughness effects

The wall functions are derived for smooth walls. However, many flows in engineering applications occur over rough surfaces. Roughness effects can increase turbulence and transport of momentum, heat and mass if the roughness is large enough. Generally three different regimes can be observed based on the dimensionless roughness height. The dimensionless roughness height is given by:

$$K^+ = \frac{\rho u_* K}{\mu} \quad (2.23)$$

It has been shown that roughness effects are negligible for K^+ -values ≤ 2.45 in the hydrodynamically smooth regime, and becomes more significant in a transitional regime as the value increases to the fully rough regime where $K^+ \geq 90$ [25].

2.3 Hydrodynamic loads on rotating cylinders

A rotating cylinder in cross-flow experiences forces due to drag and lift. A torque is also generated by friction between the rotating body and the surrounding fluid. The lift force exerted on a rotating cylinder in a moving fluid is due to the Magnus effect. The Magnus effect is caused by an acceleration of the fluid close to the cylinder body due to the no-slip boundary condition. As the fluid moves with the direction of rotation, the free stream fluid velocity accelerates on one side of the cylinder and decelerates on the other side. The acceleration and deceleration of the surrounding flow profile creates regions of low and high pressure on respective sides of the cylinder, resulting in a net lift force [27].

The force component perpendicular to the flow direction is called the lift force and is given by:

$$F_L = \frac{1}{2} C_L \rho U^2 D L \quad (2.24)$$

where C_L is the lift coefficient, U is the free-stream velocity, ρ the water density, D and L the cylinder diameter and length. The force component parallel to the flow direction is called the drag force, which is given by:

$$F_D = \frac{1}{2} C_D \rho U^2 D L \quad (2.25)$$

The friction between the rotating cylinder surface and the surrounding fluid causes a friction torque, given by:

$$M_F = \frac{1}{2} C_M \rho U^2 D L \quad (2.26)$$

The characteristics of flow past rotating cylinders are strongly dependant on the flow regime characterized by the speed ratio α and the Reynolds number. The speed ratio is the ratio of the circumferential velocity of the cylinder to the free-stream velocity and is given by:

$$\alpha = \frac{r\omega}{U_\infty} \quad (2.27)$$

where r is the cylinder radius, ω is the angular velocity and U_∞ is the free-stream velocity. The Reynolds number relates the inertial forces of the fluid flow to the viscous forces, and is given by:

$$Re = \frac{U_\infty D}{\nu} \quad (2.28)$$

2.3.1 Estimation of forces

The lift force per unit length of cylinder can be calculated for potential flow by the Kutta-Joukowski lift theorem:

$$L' = -\rho_\infty U_\infty \Gamma \quad (2.29)$$

Where L' is the lift force per unit length, ρ_∞ and U_∞ are the free stream density and velocity and Γ is the circulation defined as:

$$\Gamma = \oint_C V ds \quad (2.30)$$

The strength of the circulation can be estimated for rotating cylinders by:

$$\Gamma = r \int_0^{2\pi} r\omega d\Theta = 2\pi r^2 \omega \quad (2.31)$$

The lift coefficient can be estimated by dividing Equation 2.29 with $rU_\infty^2 \rho$:

$$C_L = \frac{\Gamma}{U_\infty r} = \frac{2\pi r\omega}{U_\infty} = 2\pi\alpha \quad (2.32)$$

The friction moment can be calculated by an empirical expression proposed by Theodorsen [9] who investigated drag on fast spinning cylinders in high Reynolds numbers flows. He proposed the following empirical correlation for the friction of a rotating cylinder:

$$M_f = C_f \pi \rho r^4 \omega^2 \quad (2.33)$$

where C_f is the skin friction coefficient given by:

$$\frac{1}{\sqrt{C_f}} = -0.6 + 4.07 \log_{10} (Re \sqrt{C_f}), \quad Re = \frac{d^2 \omega}{4\nu} \quad (2.34)$$

3

Methods

This chapter gives a description of the simulation methodology used in this study. All simulations of the hydrodynamic loads on the rotating spar were performed with CFD using the software ANSYS Fluent 19.2 and 17.2. ANSA 18.1 was used to create the geometry and mesh.

3.1 Domain

This section describes the different computational domains used for the 2D, 3D and spar simulations.

3.1.1 2D cylinder simulations

A schematic description of the 2D computational domain is given in Figure 3.1. The computational domain consists of a rectangular area with a cylinder centered between two outer symmetry boundaries. The cylinder represents a cross-section of the wind turbine spar. The cylinder is located closer to the inlet than the outlet to ensure that the turbulence intensity from the inlet remains high (the behaviour of the turbulence intensity is discussed further in Section 4.1.3), but far enough to avoid pressure effects from the inlet that could influence the force and moment coefficients. The domain should also be sufficiently long after the cylinder to capture the wake.

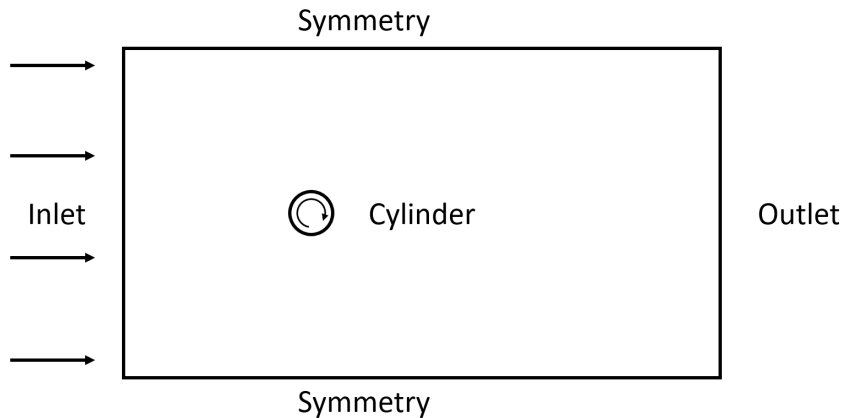


Figure 3.1: Schematic description of the 2D computational domain.

Mittal and Kumar [12] concluded that an outer boundary located $75D$ from the cylinder is enough to avoid having effects on the moments and forces from the domain size. As the cylinder diameter is in the range of 5 m, a very large domain would have been required. Three different domain sizes are therefore investigated in order to determine the minimum required domain size where coefficients are not significantly affected. The dimensions of the three domains are given in Table 3.1.

Table 3.1: Different domain sizes used for the 2D simulation.

Domain	Length and width	Distance to symmetry and inlet
1	L 250 m, W 200 m	100 m, 50 m (20D, 10D)
2	L 300 m, W 200 m	100 m, 100m (20D, 20D)
3	L 700 m, W 500 m	250m, 200m (50D, 40D)

3.1.2 3D cylinder simulations

An illustration of the 3D computational domain is given in Figure 3.2. The 3D domain consists of a rectangular cuboid with the same length and width as 2D domain 3 given in Table 3.1. The height of the domain is characterized by the cylinder aspect ratio (the ratio of the cylinder height to the diameter). Aspect ratios of 6 and 10 are investigated, with a corresponding domain height of 30 and 50 m, respectively. The boundary conditions at the sides, top and bottom are set to symmetry.

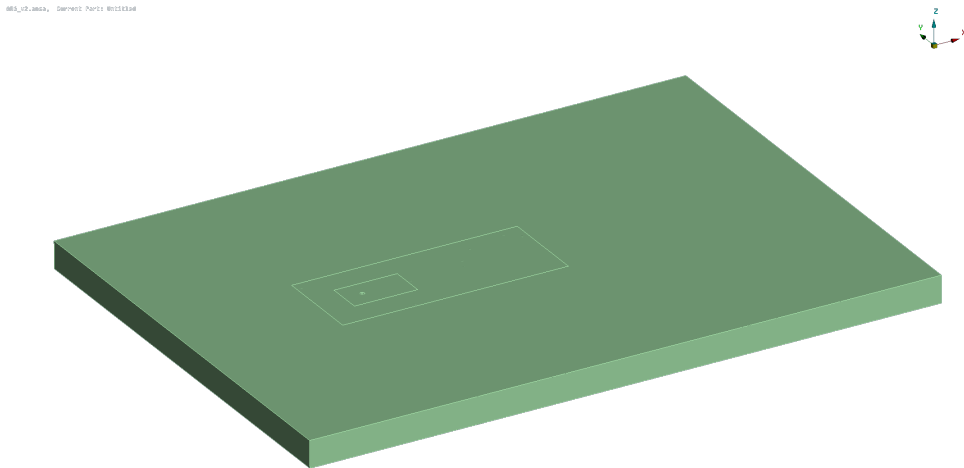


Figure 3.2: The computational domain for the 3D simulations of a cylinder.

3.1.3 3D spar simulations

Simulations of the spar are done with the same domain length and width as for the 3D cylinder. The height of the domain is 200 m, with the spar occupying the upper 80 meters. The domain extends 120 m below the spar to represent the ocean depth at the location of the wind turbine. Figure 3.3 shows the geometry of the simulated spar with names for the different sections. The top surface represents the water surface and is modeled by a free-slip wall. The bottom surface is a no-slip wall which represents the ocean floor. The inlet uses the velocity profile described in Section 3.6.

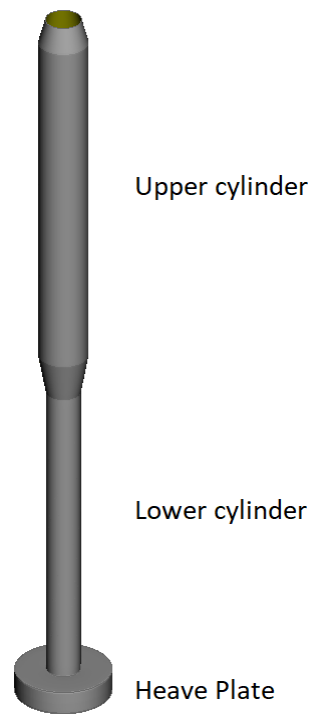


Figure 3.3: The geometry for the 3D spar with names for the different sections.

3.2 Mesh

This section describes the different meshes used for the 2D, 3D and spar simulations.

3.2.1 2D mesh

The 2D mesh consists of a triangular surface mesh with a layer of quadrilateral cells closest to the cylinder surface. The cells in the near-wall layer are grown with rate of 1.3 in 25 layers. The mesh resolution close to the cylinder is such that $y^+ < 1$ for all cells. The mesh resolution is decreased further away from the cylinder, as shown in Figure 3.4.

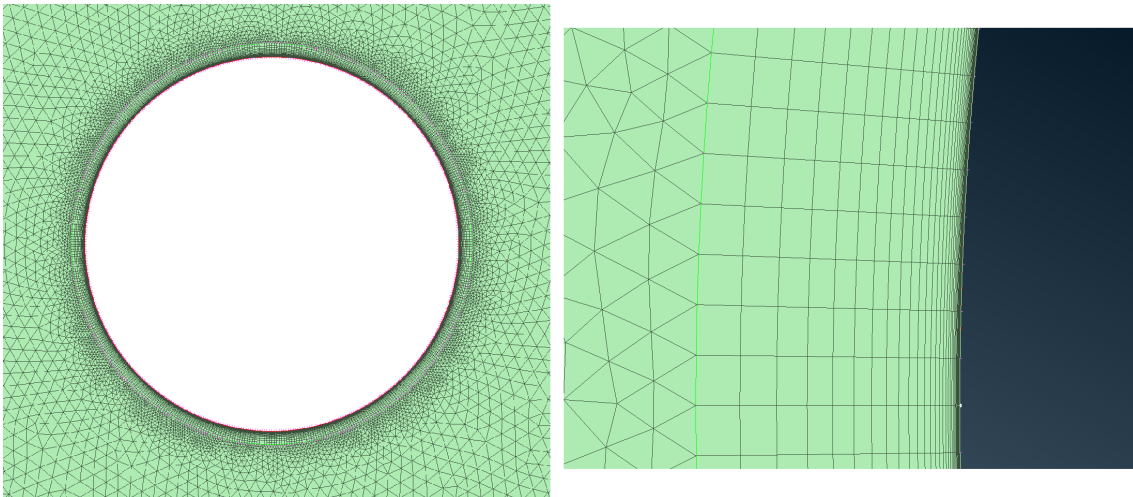


Figure 3.4: The mesh close to the cylinder, showing the prism layer and the unstructured grid.

To ensure mesh independence three different mesh resolutions are investigated. The investigated mesh sizes are summarized in Table 3.2.

Table 3.2: Different mesh sizes used for the simulations.

Mesh	Number of cells
1	150,000
2	350,000
3	850,000

3.2.2 3D mesh

The mesh for the 3D domain consists of 5.8 million cells in an unstructured tetrahedral mesh with a prism layer closest to the cylinder surface. The prism layer is used to accurately capture the boundary layer and consists of 25 layers with a growth rate of 1.2. The near wall resolution is such that $y^+ < 1$ for all cells. A cross section of the 3D mesh is shown in Figure 3.5.

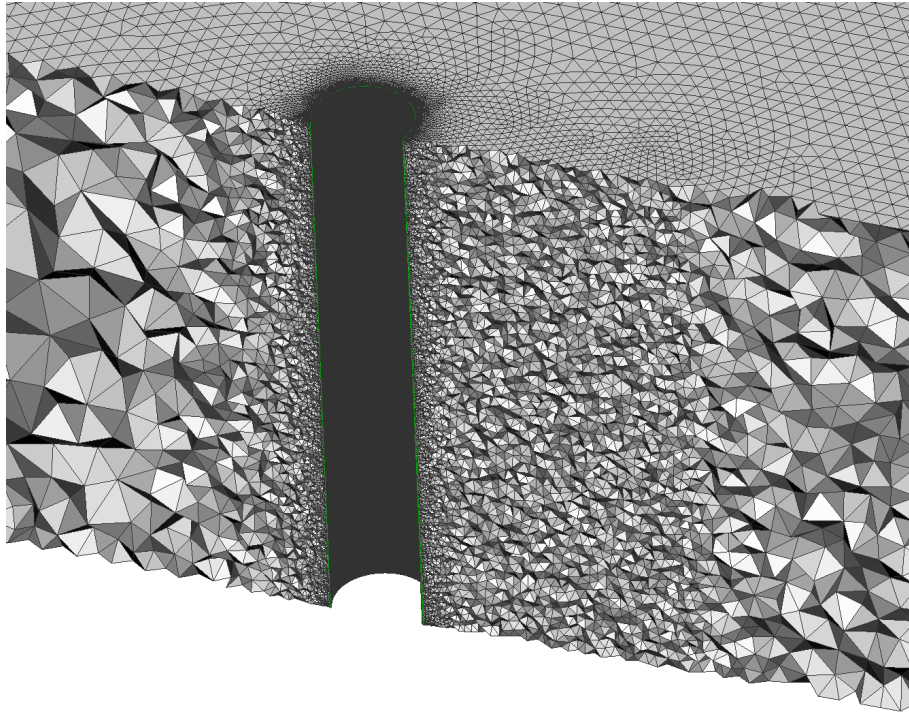


Figure 3.5: Cross-section of the 3D mesh.

3.2.3 Spar mesh

The mesh for the spar simulations consists of 18 million cells and is shown in Figure 3.6. The mesh is refined in regions close to the spar and in the wake. A 25 cells thick prism layer is used closest to the cylinder surface, with a first cell thickness of 0.02 mm, giving $y^+ < 1$ for all cells.

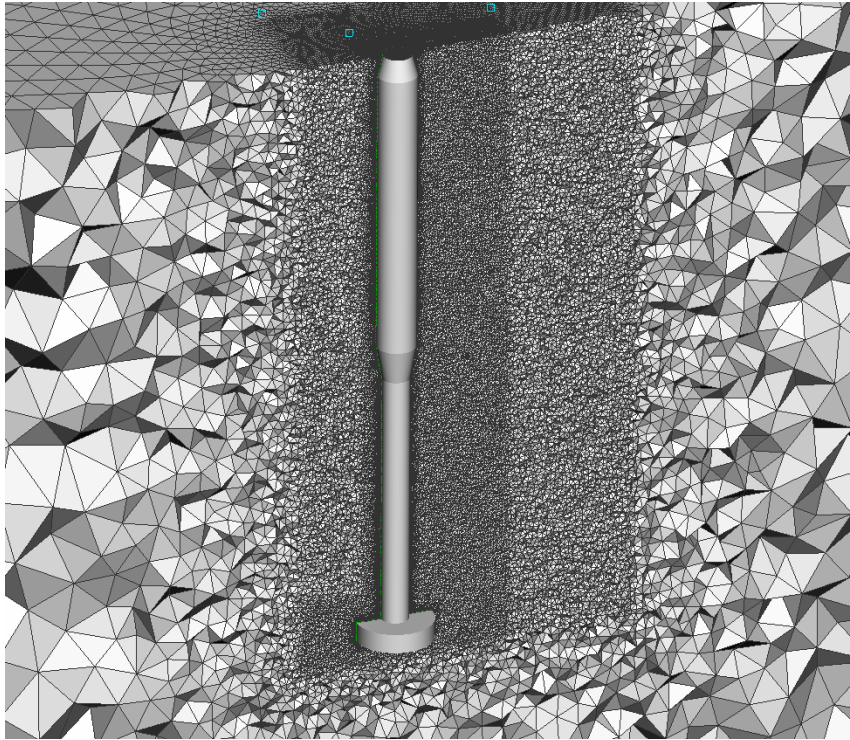


Figure 3.6: Cross-section of the spar mesh.

3.3 Simulation settings

Simulations are done with the SST $k-\omega$ turbulence model which has previously been used in similar studies by Vita [16]. Of the extra settings that are available in Fluent, the curvature correction option described in Section 2.2.6 is selected to improve the performance for swirling flows. Both steady-state and transient simulations are done. For steady-state simulations the pressure-velocity coupling is solved using a coupled solver. The coupled solver solves a coupled system of the momentum and continuity equations. This significantly decreases time for convergence at an increased memory requirement compared to a segregated solver, where the momentum and continuity equations are solved sequentially. The convective terms are discretized using a second order upwind scheme, with gradients evaluated using a least-square cell based method. To speed up simulations, transient simulations are run from an initial steady-state guess. The transient simulations use the PISO scheme for pressure-velocity coupling, as it was found to be significantly faster than the coupled scheme. A time step of 0.01 s was used with time-marching using a second order implicit scheme. The time step ensures that the convective Courant number is less than 5.

3.4 Boundary conditions

The wall boundary conditions on the cylinder are set to no-slip and zero roughness. To account for the rotation a moving wall boundary condition is also set, where the cylinder rotates around the origin with a constant velocity. The different rotational velocities are specified in rad/s and calculated from the speed ratio:

$$\omega = \frac{\alpha U_\infty}{r}$$

or from the rotations per minute (RPM) of the cylinder:

$$\omega = \frac{RPM \cdot 2\pi}{60}$$

Symmetry boundary conditions are applied on the upper and lower boundaries of the domain. The symmetry boundaries should be located sufficiently far away from the cylinder that the solution is not affected by the boundary condition. The inlet is specified as a velocity inlet with a constant velocity in the positive x-direction, and zero velocity in the y-direction. Turbulent parameters are specified by turbulent intensity and length scale. The turbulent intensity is known to decay rapidly, and as such the inlet turbulence intensity needs to be set high [25]. The outlet is specified as a pressure outlet with a backflow turbulent intensity of 5% and length scale matching the settings of the inlet.

3.5 Forces and moments

The lift, drag and friction moment coefficients are calculated from the respective forces and moments acting on the cylinder and are normalized with the cylinder diameter, length and dynamic pressure. The lift coefficient is defined as:

$$C_L = \frac{F_L}{\frac{1}{2}\rho U^2 DL} \quad (3.1)$$

The drag coefficient is defined as:

$$C_D = \frac{F_D}{\frac{1}{2}\rho U^2 DL} \quad (3.2)$$

And the friction moment coefficient:

$$C_M = \frac{M_f}{\frac{1}{2}\rho U^2 DL} \quad (3.3)$$

Where F_L , F_D and M_f are the lift force, drag force and friction moment, respectively. D and L are the cylinder diameter and length. For the 2D simulations L is set to 1 m.

3.6 Ocean current velocity profile

For the spar simulations, a velocity profile is specified for the inlet. The ocean current velocity profile presented in Figure 3.7 is based on data from the floating wind turbine Hywind demo site outside the coast of Norway, with a total depth of 210 m. The maximum 50 year extreme current value at 20 m depth is estimated to be higher than 1.4 m/s. [28]

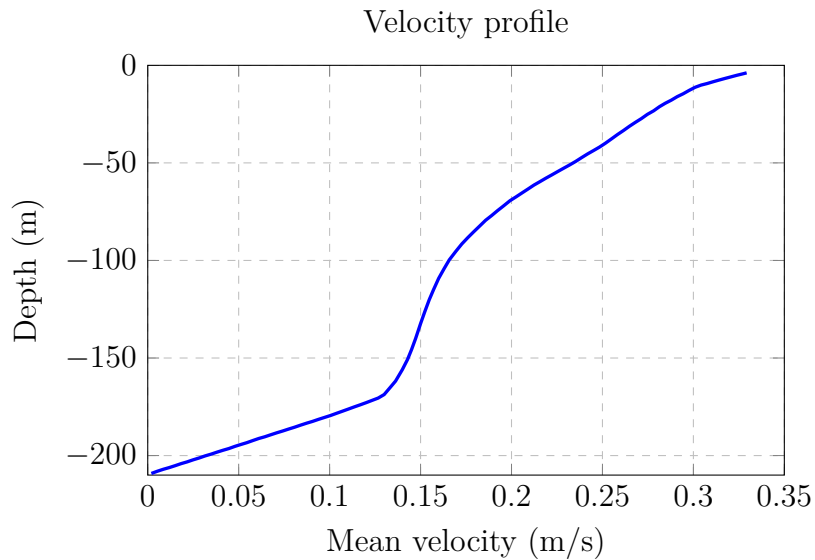


Figure 3.7: Mean current velocity as a function of water depth at the Karmøy test site. Data from [28].

4

Results and discussion

The results and discussion of the simulations using the methodology from Chapter 3 are presented in this section. The first part covers results related to the development of the 2D cylinder model. The second part covers results for the 3D cylinder model. The third part covers simulations of the spar.

4.1 2D simulations

The 2D simulations include a domain size, mesh independence and inlet turbulence intensity study. The simulations are also compared with a 2D reference case and the transient flow behaviour is evaluated.

4.1.1 Domain size

The effects of the domain size are evaluated with respect to the distance to the symmetry boundaries and from the inlet to the cylinder. The results are summarized in Figure 4.1. The lift and moment coefficients are almost unaffected by the change in domain size, with a difference of less than 4 % for all investigated speed ratios.

The drag coefficient shows a more significant variation, and is strongly affected by the distance to the inlet. The drag force becomes larger when the cylinder is located close to the inlet, which could be an effect of a pressure build-up from the stagnation point at the cylinder that extends to the inlet. The drag coefficient is also much more sensitive than the lift coefficient, as the force is approximately 30 times smaller. This means that small changes in the drag force appear as large percentual changes in the coefficient. Furthermore, differences in drag for the larger domains could be an effect of not being able to exactly recreate the turbulence intensity, as the intensity decay becomes more significant for large domains.

Taking into account the inherent uncertainties with determining the drag force, the domain is deemed sufficiently large to not influence the lift and moment coefficients at 700x400 m.

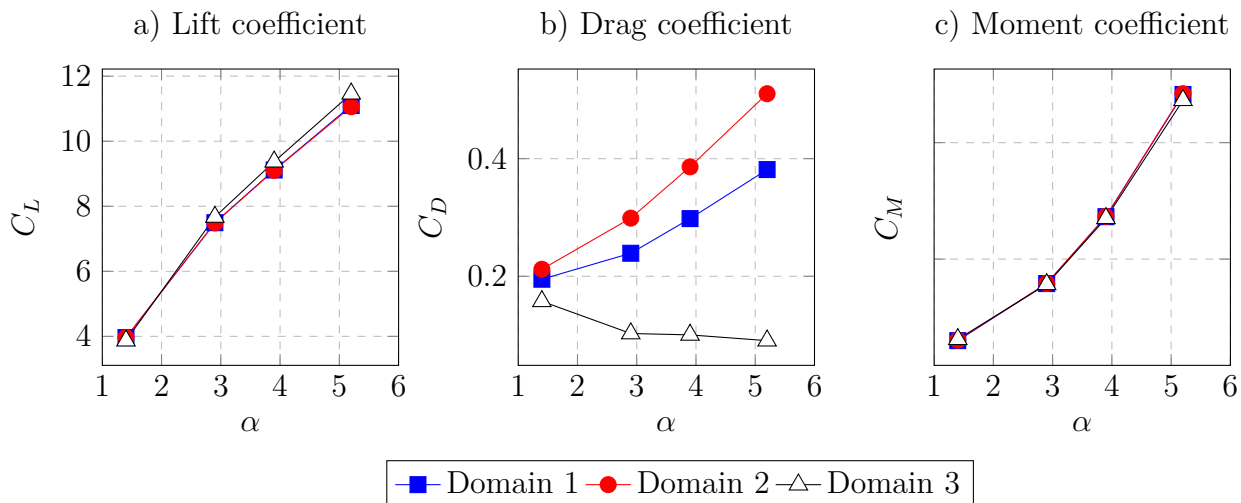


Figure 4.1: Effect of domain size on the force and moment coefficients.

4.1.2 Mesh independence

Mesh independence is investigated by comparing three different mesh resolutions (see Table 3.2) for five different speed ratios (see Table 4.3). The results are presented in Figure 4.2, which shows the force and moment coefficients plotted against the speed ratio for the different mesh resolutions. Increasing the mesh resolution above 150,000 cells does not change the lift and friction moment results in the examined speed ratio range. A slight decrease in drag occurs for the highest mesh resolution.

The solution is deemed mesh independent at 350K cells in the speed ratio range of $0 \leq \alpha \leq 5.2$. It is likely that the near wall boundary layer is already well resolved with the prism layer, and an increased free-stream resolution is not necessary to capture the forces acting on the cylinder. The mesh of 850K cells is however used for higher speed ratios to ensure a high accuracy of the results.

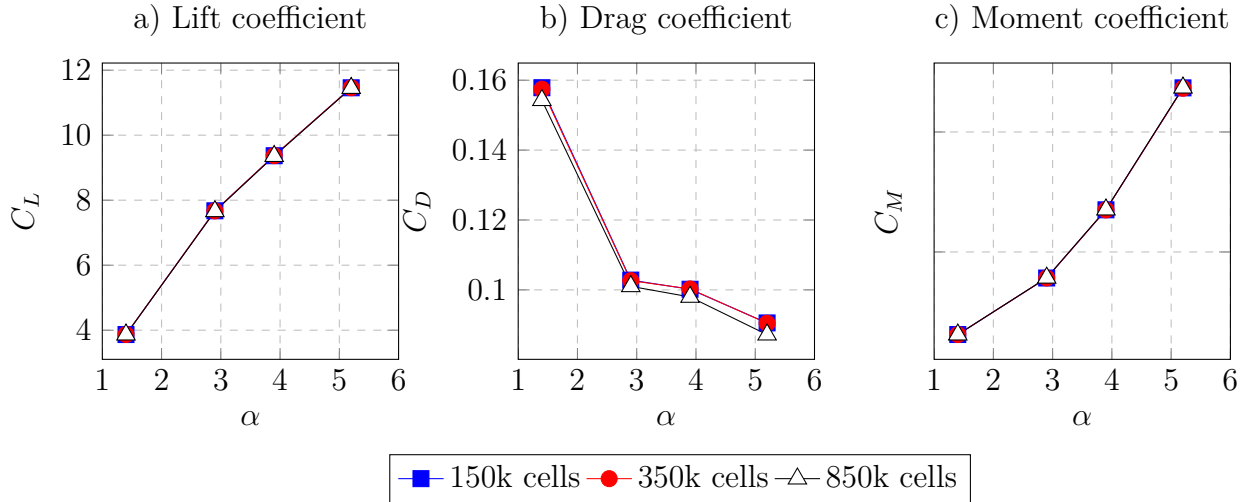


Figure 4.2: Force and moment coefficients as a function of speed ratio for different mesh resolutions.

4.1.3 Inlet turbulence intensity

The effect of the inlet turbulence boundary conditions are evaluated in terms of inlet turbulence intensity and summarized in Table 4.1. The inlet is located 200 meters upstream from the cylinder center and the turbulence length scale is set to 1.5 m. It is apparent that the turbulence intensity rapidly decreases as the flow propagates through the domain. The turbulence intensity drops to around 5 % as the flow reaches the cylinder. The drop in intensity is more significant for when the inlet turbulence intensity is set high. Examining the forces and friction moment on the cylinder, the lift force decreases with a higher turbulence intensity while the drag force and friction moment increases.

Table 4.1: Effects of changing the inlet turbulence intensity. Results are for $\alpha = 3.9$. The turbulence intensity is given at different distances from the cylinder center.

Parameter	Value		
TI, Inlet (%)	40	60	80
TI, -150 m (%)	8.77	10.52	11.81
TI, -50 m (%)	4.92	5.85	6.52
TI, -5 m (%)	4.47	5.29	5.89
C_L	9.24	8.69	8.34
C_D	0.10	0.12	0.13

Ocean turbulence is highly time and site dependant, with length-scales ranging from centimeters to hundred meters [29]. The ocean turbulent intensity has been reported in the range of 5-18 %, but is again strongly dependant on the site of measurement [29]. It can be seen that the forces and the friction varies a rather large amount

with a small change in turbulence intensity. A more accurate analysis therefore needs information of the prevailing turbulence conditions at the site of the wind turbine.

4.1.4 Comparison with reference case

Initial simulations were run for comparison with data from Vita [16], with simulations settings summarized in Table 4.2. The inlet turbulence settings are not given by Vita and are here set to 40 % turbulence intensity and 1.5 m length-scale. The 1.5 m turbulent length scale is chosen as it yields lift and friction moment results in good agreement with results by Vita. Five different speed ratios are used for evaluation as summarized in Table 4.3, matching the settings of the reference case.

Table 4.2: Boundary and operating conditions for comparison with the reference case by Vita [16].

Parameter	Value
Turbulence intensity (%)	40
Turbulent length scale (m)	1.5
Free-stream velocity (m/s)	1
Fluid dynamic viscosity (Pa s)	0.001003
Fluid density (kg/m ³)	998.2
Reynolds number	$4.985 \cdot 10^6$
Cylinder diameter (m)	5

Table 4.3: Speed ratio and angular velocity for the different simulation cases.

Case	1	2	3	4
α	1.4	2.9	3.9	5.2
ω , rad/s	0.56	1.16	1.56	2.08

A comparison of the simulation results with those of Vita is presented in Figure 4.3. It can be seen that the lift force is similarly predicted for the lowest speed ratio, but as the speed ratio is increased the model predicts an almost linear increase in lift while results from Vita level off towards $C_L=11$. The drag force results are comparable only at the lowest speed ratio. At higher speed ratios, Vita reports negative drag forces which is not the case for the 2D model. A lower drag force with an increasing α is however observed for both models. The moment coefficient correlates well, with results almost identical to the reference case.

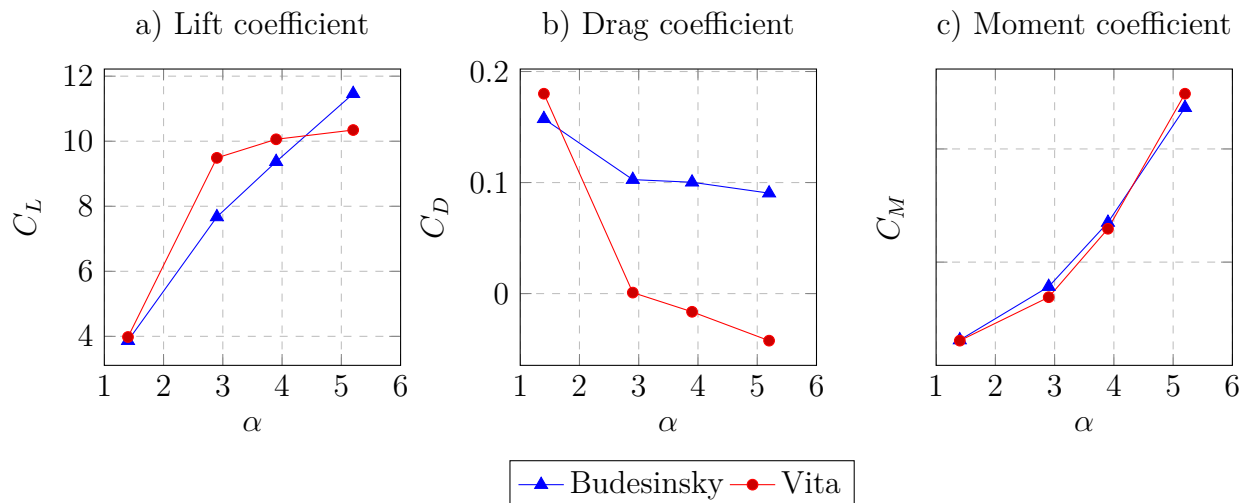


Figure 4.3: Comparison of force and moment coefficients with the reference case by Vita [16].

4.1.5 Transient flow behaviour

Simulations are started with an assumption of a steady state solution. After the steady state solution is achieved, the simulation is switched to transient to evaluate if the behaviour differs. The steady state solution generally gives a good indication if the solution is unsteady, as fluctuating residuals and forces indicate the absence of a steady-state solution. The exception is when periodic vortex shedding is present for low speed ratios, which produces a steady solution. The investigated speed ratios and corresponding angular velocity of the cylinder are presented in Table 4.4.

Table 4.4: Angular velocity for the respective speed ratios

α	ω , (rad/s)
0	0
1.4	0.56
2.9	1.16
3.9	1.56
5.2	2.08
6	2.4
7	2.8
8	3.2
10	4
12	4.8
14	5.6

The time-averaged coefficients for lift, drag and friction moment as a function of speed ratio are presented in Figure 4.4. The magnitude and time period of the

coefficient oscillations are presented in Table E.1 in Appendix E.

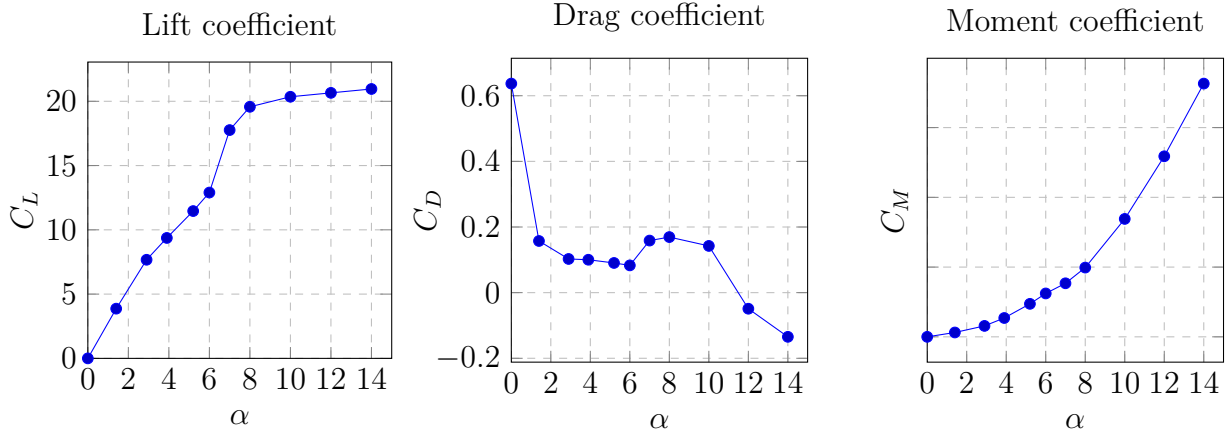


Figure 4.4: Lift, drag and moment coefficients as a function of speed ratio for the 2D CFD model.

Figure 4.5 shows a contour plot of the vorticity for different speed ratios. The vorticity describes the local spinning motion of the fluid, and is defined by the curl of the flow vector. In 2D the vorticity is given by:

$$\vec{\omega} = \frac{\partial u_y}{\partial x} - \frac{\partial u_x}{\partial y} \quad (4.1)$$

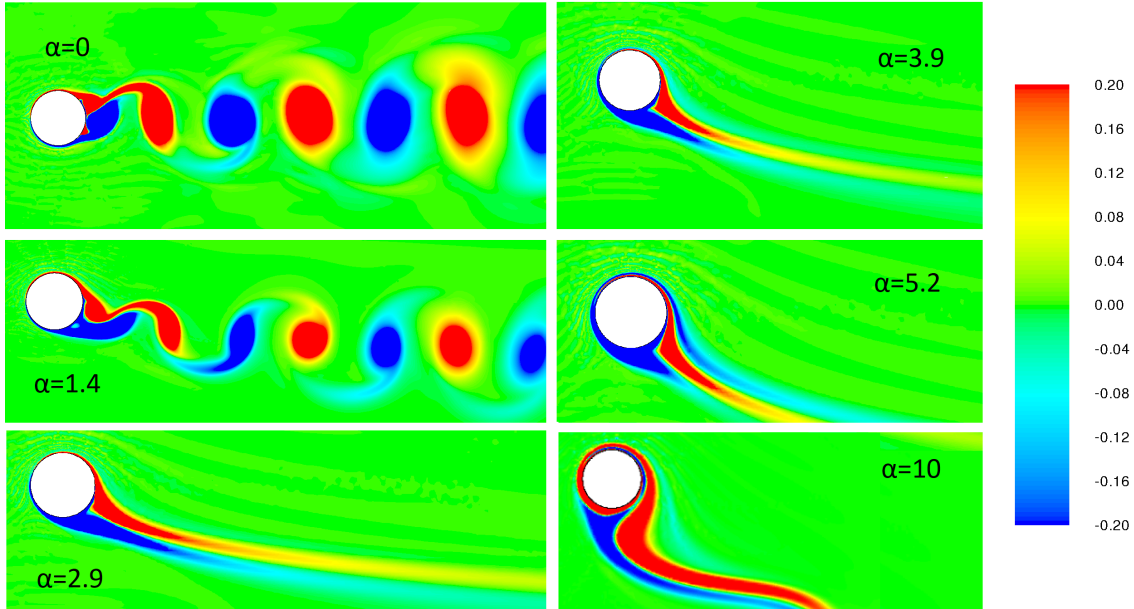


Figure 4.5: Vorticity contours for different speed ratios. Positive values (red) indicate counterclockwise rotation, negative values (blue) clockwise rotation. The flow direction is from left to right.

For the simulation case with a non-rotating cylinder a von Kármán vortex street develops, resulting in alternating negative and positive lift and drag forces. Time-averaging the forces gives a net lift force of zero, and a high drag force. The drag force is well in line with experimental data presented in Figure C.2 in Appendix C.

For a low speed ratio of $\alpha=1.4$ vortex shedding is still present. Alternating positive and negative vortices are released from the upper and lower surfaces of the cylinder, giving rise to a von Kármán vortex street in the cylinder wake. The location of the wake is shifted downwards due to the rotation of the cylinder. The alternating vortices give rise to oscillations in the lift, drag and friction moment. The rotation causes a net positive lift force and a decreasing drag compared to the stationary cylinder.

At the higher investigated speed ratios of $\alpha=2.9 - 6$, the wake is stabilized by the rotation, and the flow reaches a steady state with steady forces and moments. It can be seen that as the speed ratio increases, a steady negative vortex forms over the top positive vortex. At the same time the wake is deflected more and more in the direction of rotation.

At speed ratios of 7 and higher the flow behaviour changes. The high rotational rate causes the wake to become entrained. The vortices in the wake goes from a tail-like structure to being wrapped around the cylinder. A similar behaviour is seen for all simulations in the speed ratio range of $7 \leq \alpha \leq 14$.

Figure 4.6 shows the transient behavior of the vortex street for $\alpha = 10$. The strong rotation and viscous effects close to the cylinder causes the wake to be drawn towards the direction of rotation (A). The free-stream flow causes an elongation of the wake (B) and formation of a negative vortex, which eventually separates (C & D). The process then repeats. This type of vortex shedding is different than for a non-rotating or slowly rotating cylinder due to that only one vortex is released, and that the shedding occurs only below the cylinder. The shedding frequency is also much lower than for von Kármán shedding. The change in the wake location and structure causes a drastic change in the lift and drag forces, as shown in Figure 4.4.

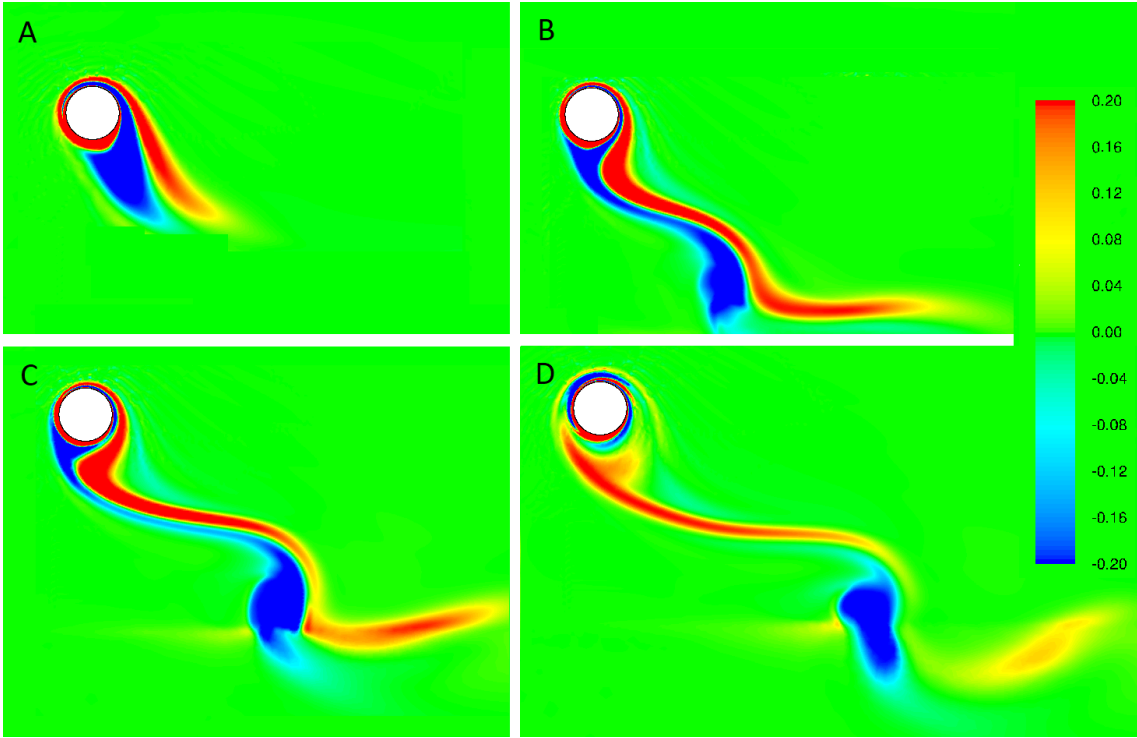


Figure 4.6: Contours of vorticity showing the development of a vortex street for $\alpha=10$.

A similar flow structure has been observed in laminar flows, although at a lower velocity ratio (Rao et al. $\alpha=6.25$ [30]). Stojković [13] also reported a second shedding mode for $\alpha = 4.35 - 5.45$ for laminar flows, with a lower shedding frequency than von Kármán shedding. The simulation drag force shows results in line with those reported by Stojković. A sudden increase in drag is seen as the speed ratio approaches the second shedding mode, followed by a sharp drop yielding negative drag forces as the second shedding mode develops. Stojković's results indicated that the onset of the second shedding mode occurs for a lower α when the Reynolds number is increased. The present results however show an onset of the second shedding mode at a higher α for a highly turbulent flow (at $\alpha=7$ for $\text{Re}=5 \cdot 10^6$).

4.1.6 Surface roughness effects

The effect of surface roughness is investigated by setting a surface roughness height to $5 \cdot 10^{-6}$, corresponding to a surface of painted steel [31]. This yields a K^+ -value of 1.3 - 6.2, meaning that the roughness is in the hydrodynamically smooth and transitional regime. Results for the simulations with surface roughness are presented in Appendix A. The addition of a surface roughness corresponding to painted steel does not seem to affect the results significantly. In the real world environment it would not be unreasonable to assume accumulation of marine growth on the spar, which would increase the surface roughness by several orders of magnitude. The

presence of marine growth is not modeled as the size of the roughness would be too large to capture while retaining the y^+ requirements of the SST $k-\omega$ model.

4.2 3D cylinder simulations

The results from the 3D simulation are expected to differ from the 2D simulations. 2D simulations often give very large lift coefficients, and there is a strong possibility that the lift forces are overestimated [14]. Furthermore, a strong dependency of the aspect ratio on the coefficients for 3D cylinders have been reported [10].

Figure 4.7 shows the force and moment coefficients for the 3D model in comparison with the 2D model. It can be seen that the two models yields similar lift coefficients in the speed ratio range of $0 \leq \alpha \leq 6$. At higher speed ratios the lift force from the 2D simulation rapidly increased while the 3D lift coefficient levels off. The friction moment is similarly predicted for all models, with the 3D simulation predicting a slightly higher friction moment for high speed ratios. The largest difference in results is visible for the drag coefficient. The 3D model gives a lower drag coefficient for a stationary cylinder but a higher drag coefficient for all speed ratios when the cylinder is rotating. The reduction in drag at $\alpha \geq 7$ is not observed for the 3D simulations. There is a possibility that the secondary shedding mode cannot develop due to the 3D instabilities. The 3D model also has a lower mesh resolution away from the cylinder due to the large computational cost, which could suppress the secondary vortices.

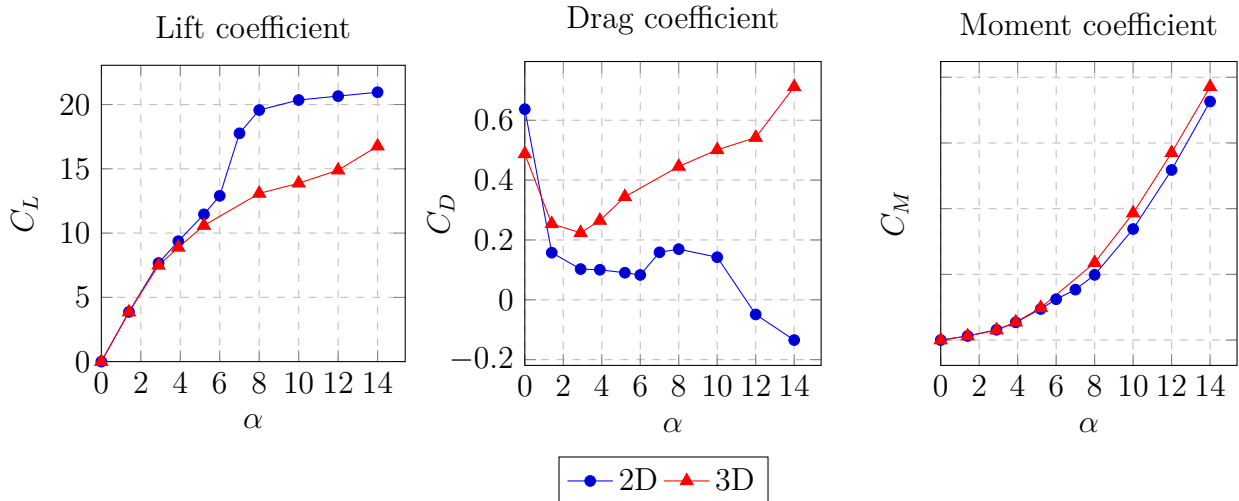


Figure 4.7: Force and moment coefficient data as a function of speed ratio for the 2D and 3D simulations.

Figure 4.8 shows an isosurface of $|\vec{\omega}| = 0.2$ coloured by 2D vorticity for a stationary cylinder. Vortex shedding similar to what can be seen in the 2D simulations is present, although the wake vortices are more uneven as a results of 3D instabilities.

Comparing the time-averaged drag coefficients for the 2D and 3D simulations in Figure C.2, it can be seen that the 3D drag coefficient is lower than for the 2D simulations and data by Tritton, but still in good agreement with experimental data by Schewe [32].

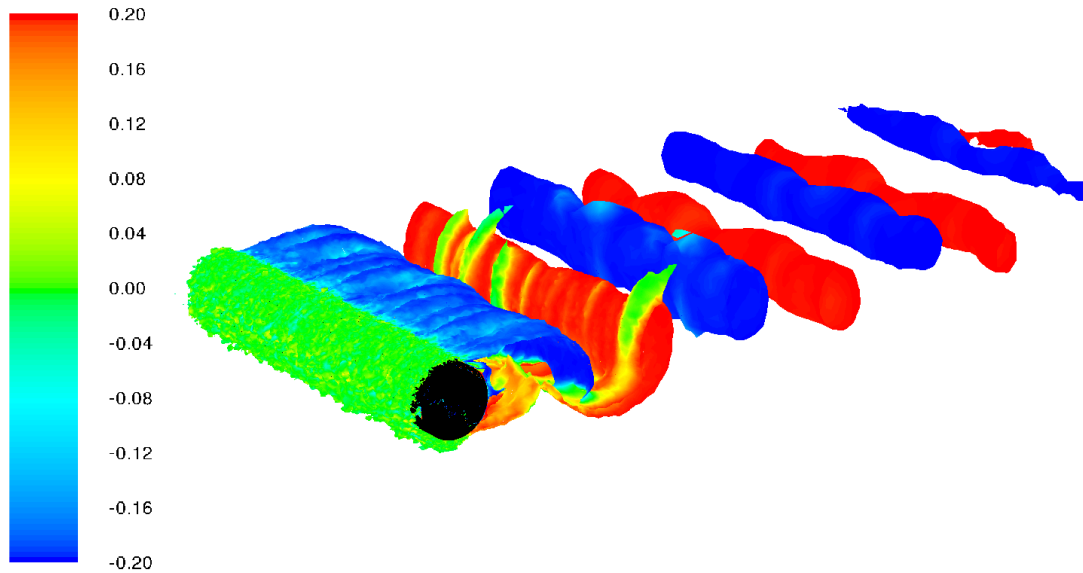


Figure 4.8: Isosurface of vorticity showing vortex shedding behind a stationary cylinder.

Isosurfaces of vorticity for different speed ratios are shown in Figure 4.9. This provides an explanation to why the 2D and 3D results differ. For low speed ratios the wake is stable and 3D effects are not pronounced, yielding a flow behaviour resembling that of the 2D case. At higher speed ratios the three-dimensional effects introduce flow instabilities which decrease lift and increase drag, as discussed by Mittal [14]. Ring-like vortices are formed along the length of the cylinder and grow in size as the rotational rate is increased, further reducing lift and increasing drag and friction.

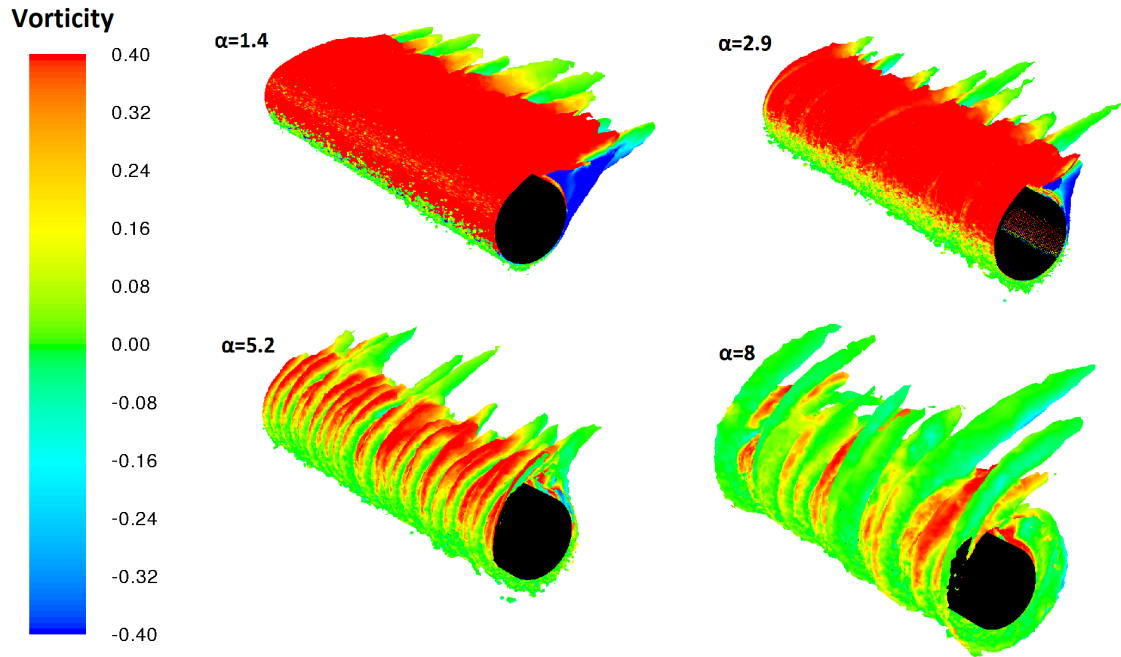


Figure 4.9: Isosurface of vorticity ($|\vec{\omega}| = 0.4$) around a rotating cylinder.

As the three-dimensional instabilities grow large in size for high speed ratios two different aspect ratios of the cylinder are investigated. This to ensure that the cylinder length is not limiting the development of the vortex structures and affecting the flow behaviour. Figure D.1 in Appendix D shows the resulting lift, drag and moment coefficients for 3D simulations of a cylinder with aspect ratio 6 and 10. There is only a very small difference in the observed coefficients for the different aspect ratios.

Figure 4.10 shows an isosurface of vorticity for the two different aspect ratios at $\alpha = 14$. Both simulations show similar results in the vortex structures along the cylinder, and the cylinder length at AR=6 does not seem to limit the development of vortex structures. Based on this, together with the small differences in results given in Figure D.1, an aspect ratio of 6 is deemed large enough to capture the most important characteristics of the flow.

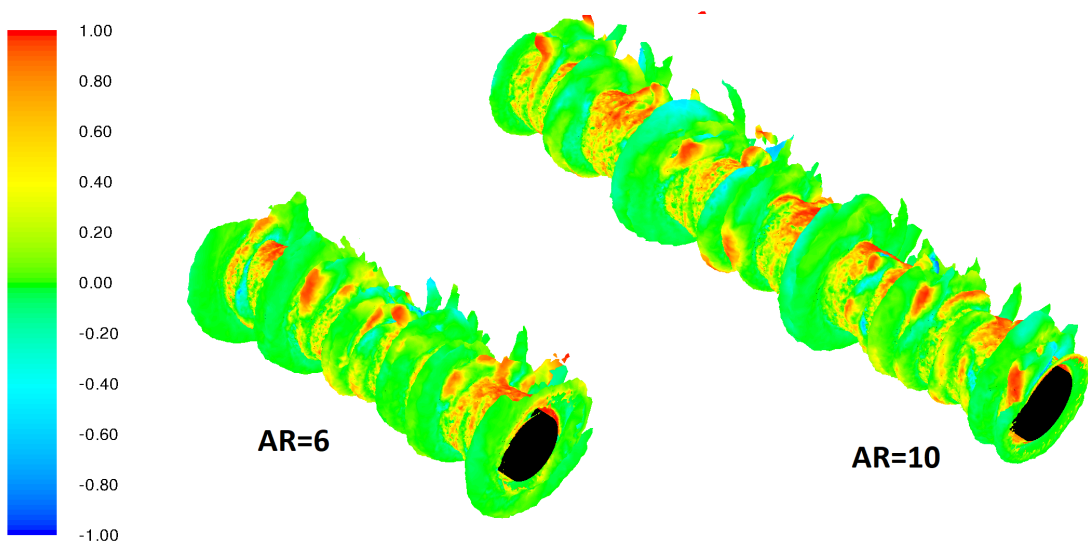


Figure 4.10: Isosurface of vorticity ($|\vec{\omega}| = 1$) for $\alpha = 14$ and two different cylinder aspect ratios. Coloured by 2D vorticity.

4.3 Model evaluation

Figure 4.11 shows a comparison of the lift force plotted against speed ratio with results from the 2D and 3D simulations, and experimental results by Tokumaru [10], Carstensen [11] and Reid [6]. Within the examined range of $\alpha=1.4 - 6$ both the 2D and 3D models predicts the lift coefficient reasonably well. For the lowest speed ratios the lift coefficient is slightly overestimated.

The predicted lift from the 2D simulation increases rapidly as the speed ratio is increased above 6. The simulation results predict far higher lift coefficients than those reported by Tokumaru [10]. The most probable cause is that 3D effects such as instabilities and flow separation are not captured, as discussed by Mittal [14]. These effects would have been present in the experimental setup by Tokumaru, leading to a lower observed lift force compared to a purely two-dimensional flow.

The 3D model generally shows a good agreement with experimental data, although the lift coefficient is underestimated for $\alpha \geq 6$. The slightly lower lift coefficient could be attributed to two major differences in the CFD model compared to experimental results. Firstly, the CFD simulations are done at a significantly higher Reynolds number than the experimental measurements. Secondly, there is a probability that the turbulence in the CFD simulation is higher due to the large length scales and high intensity specified in the inlet. It is therefore not unreasonable that the 3D model predicts a lower lift coefficient than the experimental data.

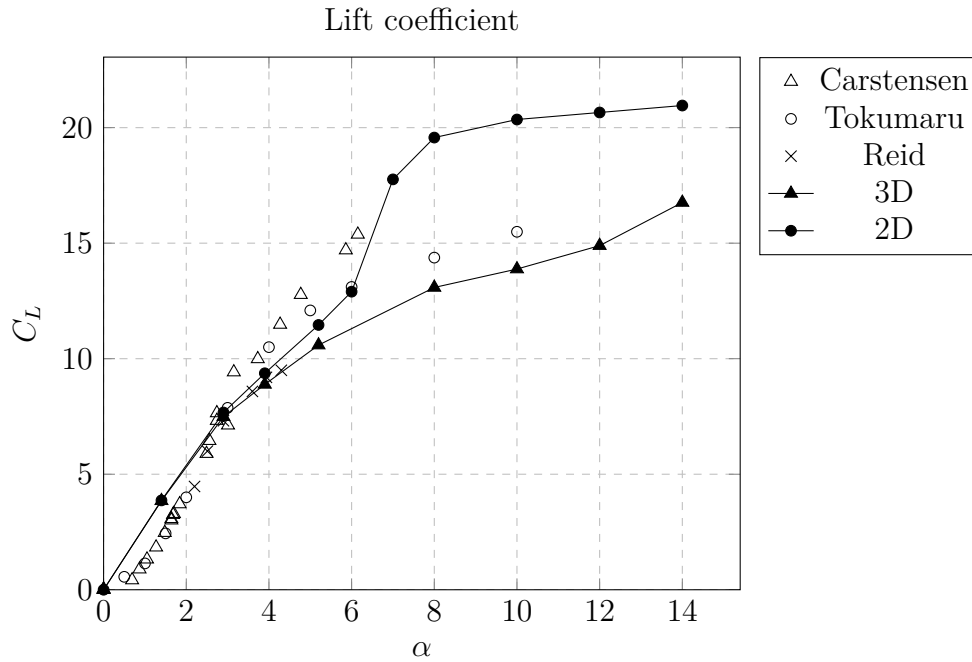


Figure 4.11: C_L as a function of speed ratio. Data from Tokumaru [10], Carstensen [11] and Reid [6].

Figure 4.12 shows the friction moment results for the 2D and 3D simulations and data from the empirical correlation by Theodorsen given by Equation 2.33. For low speed ratios the friction is relatively well correlated. For higher speed ratios the friction is however slightly underestimated. This could mean that less fluid follows the cylinder rotation, and could indicate an underestimation of lift as well.

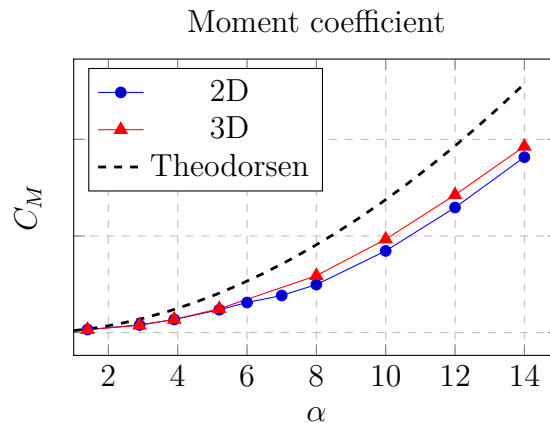


Figure 4.12: Friction moment coefficient as a function of speed ratio. The dashed line shows data obtained from the correlation by Theodorsen.

4.4 Spar simulation

This section covers simulations using the spar geometry described in Section 3.1.3. Two simulations are done, using a uniform and an ocean current velocity profiles.

4.4.1 Simulations with constant velocity

For comparison with the other models, the spar simulation was first run with a constant velocity profile. The simulations are done with a constant velocity of 1 m/s and a rotational rate of 1.204 rad/s (11.5 RPM). Due to time constraints only one rotational rate was investigated. The model is evaluated by comparing the coefficients for the two cylinder sections (the "upper cylinder" and "lower cylinder", see Figure 3.3) to results of the 2D and 3D simulations. Using a constant flow velocity is to ensure that the results are not dependent on the Reynolds number. The simulation reached steady state with stable forces over time. The resulting force and moment coefficients are reported in Figure 4.13. The lift and moment coefficients for the two sections are in agreement with results from the 2D and 3D models. The drag coefficient is however larger for both sections, and significantly larger for the upper cylinder.

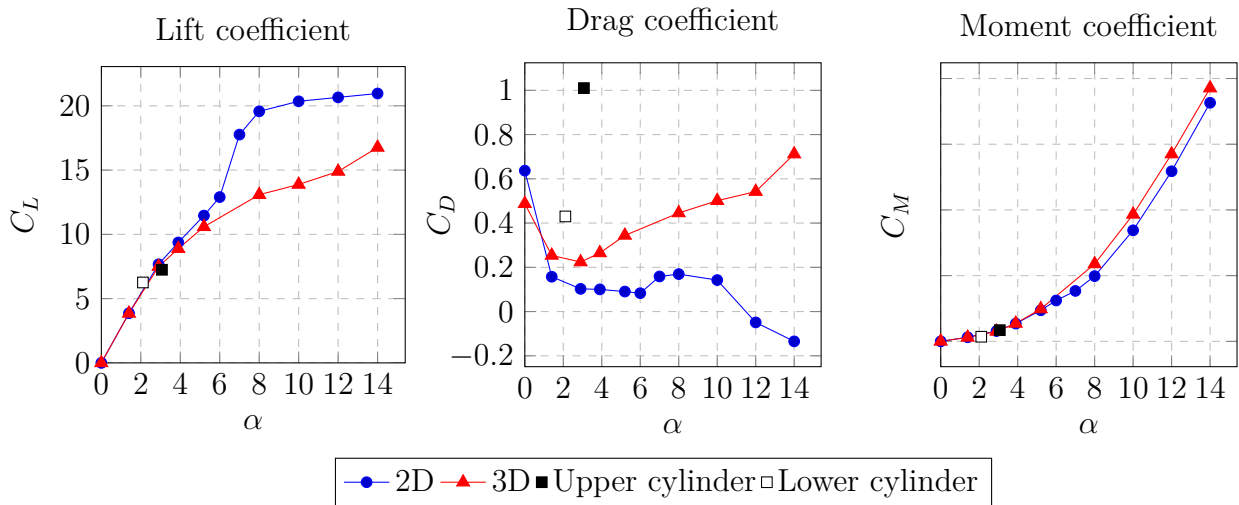


Figure 4.13: Comparison of force and moment coefficient for the different models.

4.4.2 Simulations in operating conditions

The whole spar was simulated using the flow velocity profile given in Section 3.6, corresponding to average real-world flow conditions at the site of the wind turbine. This serves to give an estimate of the forces acting on the spar under typical operating conditions. The rotational speed of the spar is set to 11.5 RPM, which is

the maximum operating speed. The simulations are run over a period of 1800 s to obtain instantaneous and time-averaged forces and moments.

Figure 4.14 shows the time history of the lift and drag forces acting on the spar. The simulations are started from a steady-state approximation to speed up convergence. The forces show oscillations with varying amplitudes and periods with a peak variation of 4.4 kN for the lift force and 2.5 kN for the drag force. The friction moment has a peak variation of kNm.

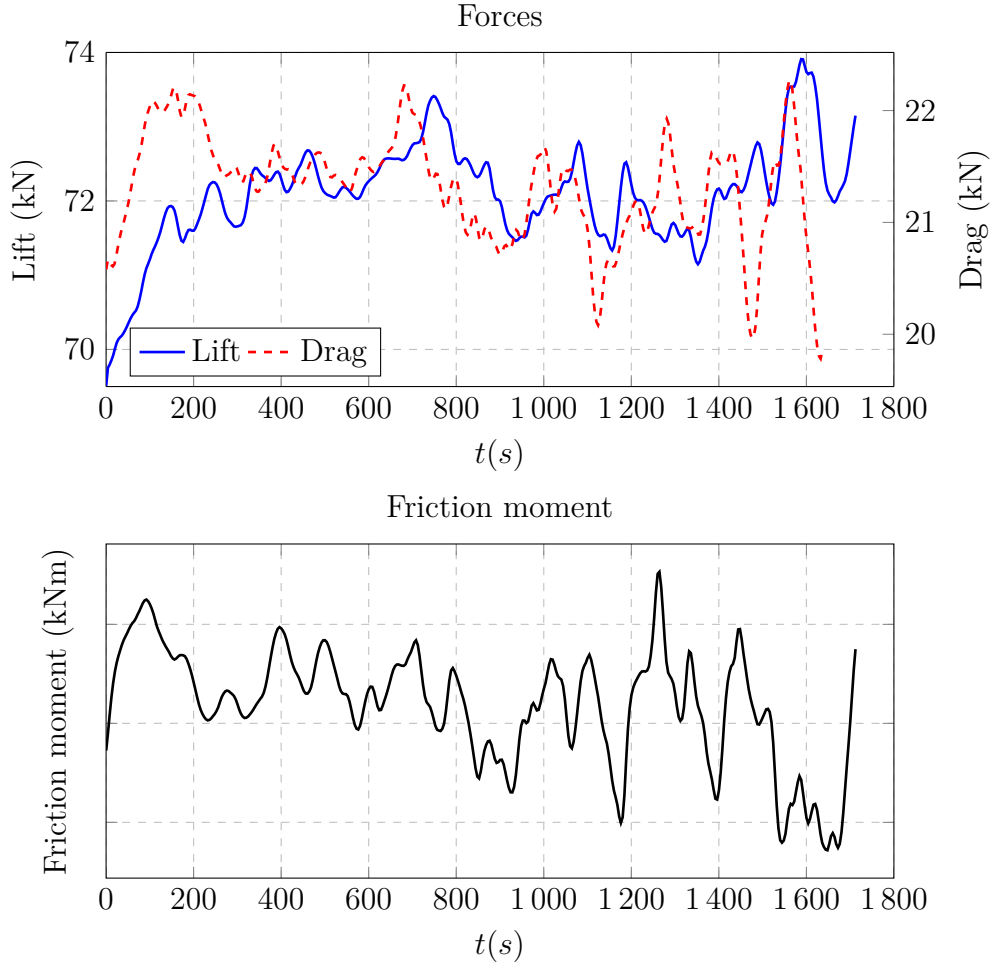


Figure 4.14: Time history for the lift, drag and friction moment acting on the spar.

The unsteady behaviour of the forces can partly be attributed to the formation of flow instabilities along the spar length. The instabilities are visible in Figure 4.15 which shows a iso-surface of vorticity ($|\omega| = 0.35$). Ring-like vortices are seen forming on the spar, which slowly move up and down the spar axis and merge over time. Due to the relatively low flow velocity and rotational rate the instabilities are still relatively stable compared to those seen in the 3D cylinder simulations. Vortex shedding is only seen close to the water surface and at the heave-plate and not along the middle section of the spar. This could explain why the fluctuations in the forces

are smaller than those seen in the 3D or 2D simulations, where vortex shedding along the whole length was present. Another reason for the smaller fluctuations could be the lower Reynolds number due to the lower flow velocity.

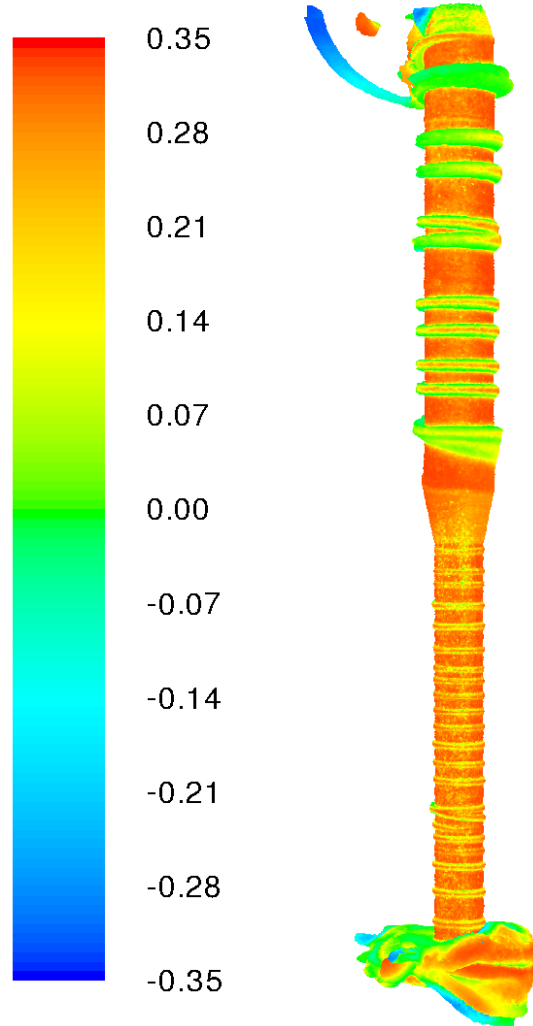


Figure 4.15: Isosurface of vorticity coloured by 2D-vorticity. Flow direction from right to left.

Figure 4.16 shows the deviation from the time-averaged mean lift force for the different sections. From this figure the contribution of the force fluctuations for each part can be assessed. It can be seen that the fluctuations of the total force are mainly dependant on the heave plate and to a lesser extent the upper cylinder. The heave plate causes the formation of a large vortex structure as seen in Figure 4.15, which causes large fluctuations in lift force.

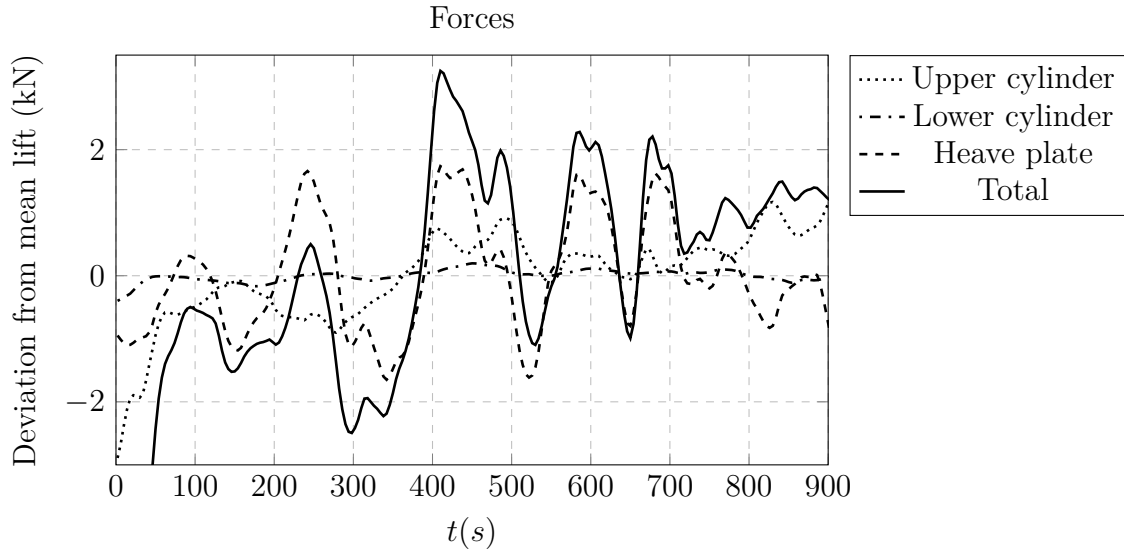


Figure 4.16: Time history of the deviation from mean lift in kN for the spar sections.

The time-averaged forces and moments are presented in Table 4.5. The total forces are presented along with forces and average coefficients acting on different sections of the spar. The power losses from friction are estimated by:

$$P = M_f \cdot \omega \quad (4.2)$$

Examining the forces, it can be seen that the upper cylindrical section contributes significantly to the lift and drag force of the spar, both due to the higher current velocity close to the water surface and due to the large projected area. The lower cylinder section contributes with roughly one fifth of the total lift and drag force. The heave plate does not provide any significant mean lift or drag, but stands for a majority of the friction moment and power losses due to the high tangential velocity at the perimeter which is a result of the large diameter. The total time-averaged forces acting on the spar are 71k N lift and 21 kN drag.

Table 4.5: Time-averaged forces, moments and friction losses for different spar sections.

Parameter	Upper cylinder	Lower cylinder	Heave plate	Total
Lift (kN)	54.69	16.41	-0.25	70.85
Drag (kN)	15.18	4.55	1.13	20.85

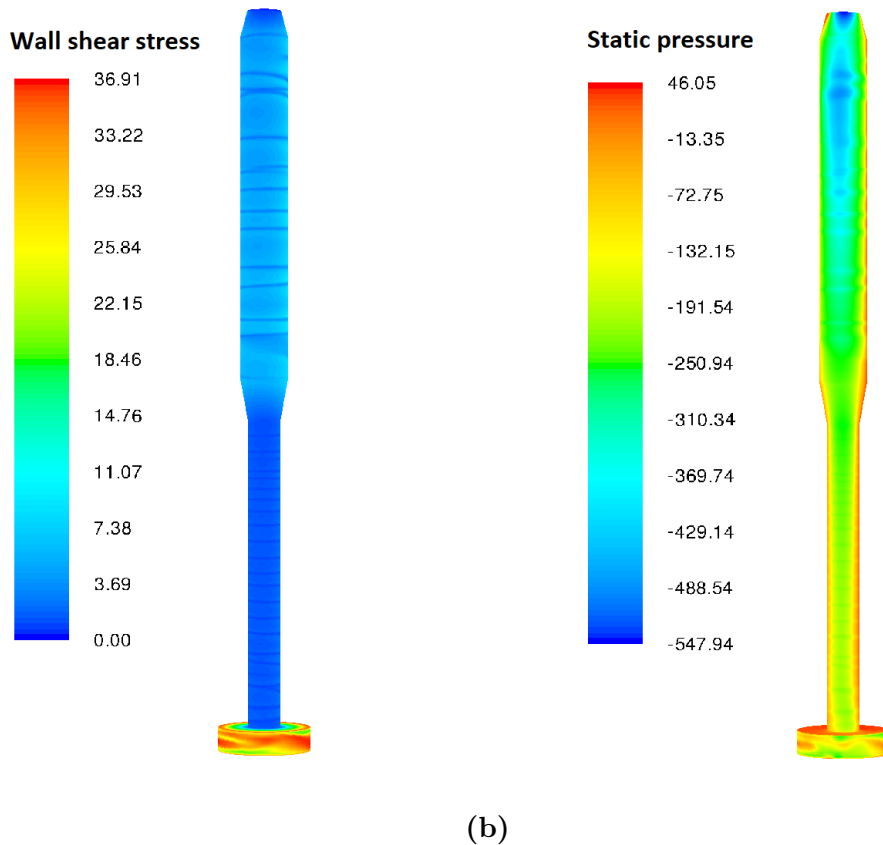


Figure 4.17: Contours of wall shear stress (4.17a) and static pressure (4.17b) on the spar. Flow direction from right to left.

The wall shear stress is shown in Figure 4.17a. The highest the shear stress is at the outer surface of the heave plate, due to the high tangential velocity. The large shear stress is the reason for the high friction torque. Figure 4.17b shows the static pressure on the cylinder. Regions of low pressure are due to the Magnus effect and are responsible for the lift force acting on the spar. The regions of lowest pressure are located mostly towards the top most part of the spar, with a center of pressure at -30 m from the water surface. This shows that the lift force will be centered slightly above the center of the spar.

The results presented in this section should give a rough approximation of the forces in operating conditions. The reader should however be aware of the many simplifications that have been made in the analysis. Firstly, the analysis is entirely static and does not consider any dynamic effects which may be present due to spar motion or pitch angle induced by the hydrodynamic or aerodynamic loads. Secondly, the flow field and velocity profile is assumed to be steady and flows only in one direction. The dynamic effect of waves is not accounted for and the turbulence settings may not be representative for the location of the wind turbine. It is possible that marine growth could influence the magnitude of the drag and lift forces, and it is not unreasonable to assume that the friction losses could increase.

4.5 Comparison of force estimations

An estimation of the total forces acting on the spar is done using the coefficient data from the 2D and 3D simulations presented in Figure 4.7. The estimation is simplified by assuming that the spar consists of two cylindrical sections with constant diameter. The two sections are each 40 m long with a 5.1 and a 3.5 m diameter, respectively. The heave-plate is omitted from the estimation as the data is only valid for rotating cylinders, and speed ratio for the heave-plate ($\alpha \approx 30$) is outside of the data range.

The forces are calculated per unit length by Equations 2.24-2.26, using a piecewise linear function between coefficient data points and the velocity profile in Figure 3.7. The unit length forces are then integrated along the spar length, with the resulting forces presented in Table 4.6 for a uniform velocity profile of 1 m/s and in Table 4.7 for the ocean velocity profile.

Table 4.6: Estimations of forces acting on the spar based on different simulation models for a uniform velocity profile ($U = 1$ m/s).

Model	Lift, kN	Drag, kN
2D	1208.37	19.64
3D	1178.01	40.32
Spar	938.69	118.73

Table 4.7: Estimations of forces acting on the spar based on different simulation models using an ocean current velocity profile.

Model	Lift, kN	Drag, kN
2D	241.7	1.1
3D	167.1	6.0
Spar	70.9	20.9

For a uniform velocity profile all three models give lift force results in roughly the same order of magnitude. The drag force shows a large difference between the models, and cannot be accurately determined or validated due to limited experimental data. The friction losses are mainly governed by the heave-plate and are therefore not very well captured with just a cylinder simulation. The estimation of forces with the ocean current velocity profile shows much larger variations between the models. This is partly a result of the large differences in coefficient data for high speed ratios. Moreover, the 3D effects of using a velocity profile have not been evaluated.

5

Conclusion

A CFD model for simulating the hydrodynamic forces on 2D and 3D cylinders have been developed and validated with published experimental data. The results from the 2D simulation showed good agreement with experimental data in the speed ratio range of $\alpha=0-6$ for the lift coefficient, but overestimated lift for higher speed ratios. The stability of the wake was found to be highly dependant on the speed ratio, with von Kármán vortex shedding developing for $\alpha=0-1.4$ which ceased at $\alpha=2.9-7$ as the flow stabilized. For $\alpha \geq 7$ a secondary type of vortex shedding different from the von Kármán shedding was observed.

The 3D model yielded similar results as the 2D simulation for $\alpha=0-5.2$, but showed a less pronounced increase in lift for higher speed ratios, which was attributed to the development of 3D instabilities along the cylinder axis, resulting in a decreased lift and increased drag. The secondary shedding mode was not observed for the 3D simulations. The lower increase in lift coefficient for high speed ratios was more in line with the trend seen for experimental data, although the lift coefficient for the 3D simulations was slightly lower. This was attributed to the higher Reynolds number and turbulence in the simulation compared to experimental measurements. Both the 2D and 3D models predicted the friction moment well.

Finally, a simulation model for the rotating spar was developed based on the results, boundary and operating conditions of the 2D and 3D simulations. The simulation of the spar in operating conditions yielded forces amounting to 71kN lift and 21 kN drag. The friction losses amounted to kW. It was found that a majority of the lift comes from the upper spar section and that the heave plate contributed to most of the friction losses and fluctuations in forces. In conclusion, the lift and friction moment seems to be captured well for the different models, while the estimation of drag is uncertain due to the lack of experimental data.

6

Recommendations for further work

The limitations of the simulation model have been discussed. Ultimately, experimental data from a scale model would be needed to completely validate the accuracy of the simulation model.

Furthermore, more numerical studies could be done. As the 2D and 3D simulations are done using only one velocity, further simulations should be done to evaluate the effect of the Reynolds number. The differences in results when using a velocity profile could also be further investigated. It can be assumed that the surface roughness would increase from marine growth, and a further study of how this would affect the results could be of interest. Lastly, the effect of an incline of the cylinder is not accounted for, which could be investigated by static or dynamic simulations.

References

- [1] European Commission. *A policy framework for climate and energy in the period from 2020 to 2030*. 2014.
- [2] E. Hau. *Wind turbines: fundamentals, technologies, application, economics*. New York : Springer, 2013.
- [3] Ivan Komusanac, Daniel Fraile, and Guy Brindley. *Wind energy in Europe in 2018, Trends and statistics*. Tech. rep. 2019.
- [4] Ki-Yong Oh, Woochul Nam, Moo Sung Ryu, Ji-Young Kim, and Bogdan I. Epureanu. “A review of foundations of offshore wind energy convertors: Current status and future perspectives”. *Renewable and Sustainable Energy Reviews* 88 (2018), pp. 16–36.
- [5] SeaTwirl AB. *SeaTwirl S2*. 2019. URL: <https://seatwirl.com/products/seatwirl-s2/> (visited on 02/20/2019).
- [6] Elliott G Reid. “Tests of Rotating Cylinders.” (1924).
- [7] L Prandtl. “Application of the "Magnus effect" to the Wind Propulsion of Ships.” *Die Naturwissenschaft* 13 (1926), pp. 93–108.
- [8] A Thom. “Effect of discs on the air forces on a rotating cylinder” (1934).
- [9] Arthur Regier and Theodore Theodorsen. “Experiments on Drag of Revolving Disks, Cylinders, and Streamline Rods at High Speeds.” (1944).
- [10] P. T. Tokumar and P. E. Dimotakis. “The lift of a cylinder executing rotary motions in a uniform flow.” *Journal of fluid mechanics*. 1993.
- [11] Stefan Carstensen. *Technical Report on the Physical Model Experiments*. Tech. rep. 2012.
- [12] Sanjay Mittal and Bhaskar Kumar. “Flow past a rotating cylinder”. *Journal of Fluid Mechanics* 476 (2003), pp. 303–334.
- [13] D. Stojković, P. Schön, M. Breuer, and F. Durst. “On the new vortex shedding mode past a rotating circular cylinder”. *Physics of Fluids* 15.5 (2003), pp. 1257–1260.
- [14] Navrose Navrose, Jagmohan Meena, and Sanjay Mittal. “Three-dimensional flow past a rotating cylinder”. *Journal of Fluid Mechanics* 766 (2015), pp. 28–53.
- [15] S.J. Karabelas. “Large Eddy Simulation of high-Reynolds number flow past a rotating cylinder”. *International Journal of Heat and Fluid Flow* 31.4 (2010), pp. 518–527.
- [16] Luca Vita. “Offshore Floating Vertical Axis Wind Turbines with Rotating Platform”. PhD thesis. Danish Technical University, 2011.

-
- [17] S.J. Karabelas, B.C. Koumroglou, C.D. Argyropoulos, and N.C. Markatos. “High Reynolds number turbulent flow past a rotating cylinder”. *Applied Mathematical Modelling* 36.1 (2012), pp. 379–398.
- [18] Takeo Kajishima and Kunihiko Taira. *Computational Fluid Dynamics: Incompressible Turbulent Flows*. Springer International Publishing, 2017.
- [19] Jiri Blazek. “Chapter 7 - Turbulence Modeling”. *Computational Fluid Dynamics: Principles and Applications (Third Edition)*. Ed. by Jiri Blazek. Third Edition. Oxford: Butterworth-Heinemann, 2015, pp. 213–252.
- [20] W.P. Jones and B.E. Launder. “The calculation of low-Reynolds-number phenomena with a two-equation model of turbulence”. *International Journal of Heat and Mass Transfer* 16.6 (1973), pp. 1119–1130.
- [21] Florian R. Menter. “Zonal Two Equation Kappa-Omega Turbulence Models for Aerodynamic Flows.” *AIAA Fluid Dynamics Conference* (1993).
- [22] David C. Wilcox. “Formulation of the $k-\omega$ Turbulence Model Revisited.” *AIAA Journal* 46.11 (2008), p. 2823.
- [23] P.R. Spalart and M. Shur. “On the sensitization of turbulence models to rotation and curvature”. *Aerospace Science and Technology* 1.5 (1997), pp. 297–302.
- [24] Pavel E. Smirnov and Florian R. Menter. “Sensitization of the SST Turbulence Model to Rotation and Curvature by Applying the Spalart—Shur Correction Term.” *Journal of Turbomachinery* 131.4 (2009).
- [25] *ANSYS Fluent 17.2 Theory Guide*. ANSYS, Inc. 2600 ANSYS Drive, Canonsburg, PA 15317, 2016.
- [26] Bengt Andersson, Ronnie Andersson, Love Håkansson, Mikael Mortensen, Rahman Sudiyo, and Berend van Wachem. *Computational fluid dynamics for engineers*. Cambridge ; New York : Cambridge University Press, 2012.
- [27] Jost Seifert. “A review of the Magnus effect in aeronautics”. *Progress in Aerospace Sciences* 55 (2012), pp. 17–45.
- [28] Anja Eide Onstad, Marit Stokke, and Lars Sætran. “Site Assessment of the Floating Wind Turbine Hywind Demo”. *Energy Procedia* 94 (2016). 13th Deep Sea Offshore Wind R&D Conference, EERA DeepWind’2016, pp. 409–416.
- [29] I.A. Milne, A.H. Day, R.N. Sharma, and R.G.J. Flay. “The characterisation of the hydrodynamic loads on tidal turbines due to turbulence”. *Renewable and Sustainable Energy Reviews* 56 (2016), pp. 851–864.
- [30] A. Rao, A. Radi, J.S. Leontini, M.C. Thompson, J. Sheridan, and K. Hourigan. “A review of rotating cylinder wake transitions”. *Journal of Fluids and Structures* 53 (2015). Special Issue on Unsteady Separation in Fluid-Structure Interaction–II, pp. 2–14.
- [31] *Environmental conditions and environmental loads*. Tech. rep. Det Norske Veritas, Oct. 2010.
- [32] Günter Schewe. “On the force fluctuations acting on a circular cylinder in crossflow from subcritical up to transcritical Reynolds number”. *Journal of Fluid Mechanics* 133 (Aug. 1983), pp. 265–285.
- [33] D. J. Tritton. *Physical fluid dynamics*. The Modern university physics series. Van Nostrand Reinhold Co., 1977.

A

Appendix: Surface roughness effects

The effect of adding a surface roughness corresponding to painted steel ($5 \cdot 10^{-6}$ m) to the 2D cylinder simulations is presented in Table A.1.

Table A.1: Effect of surface roughness on the coefficients.

C_L			
α	Rough	Smooth	Change (%)
1.4	3.86	3.87	-0.25
2.9	7.68	7.67	0.10
3.9	9.39	9.37	0.19
5.2	11.50	11.46	0.39
C_D			
α	Rough	Smooth	Change (%)
1.4	0.16	0.16	0
2.9	0.10	0.10	0
3.9	0.10	0.10	0
5.2	0.09	0.09	0
C_M			
α	Rough	Smooth	Change (%)
1.4			1.63
2.9			1.57
3.9			1.88
5.2			2.02

B

Appendix: Potential flow theory

Figure B.1 shows the predicted lift coefficient for potential flow theory. C_L is calculated from Equation 2.32. The Kutta-Joukowski lift theorem strongly overestimates the lift force compared to both the 2D and 3D models.

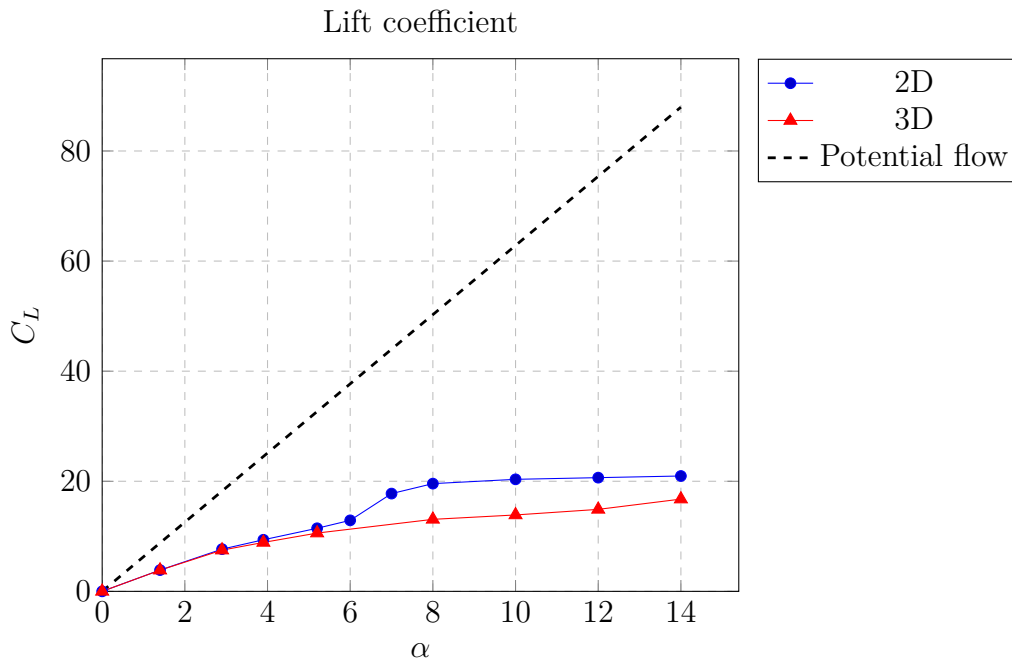


Figure B.1: Lift coefficient predicted by potential flow theory compared to the CFD results.

C

Appendix: Summary of experimental data

The experimental data for the lift coefficients available in the literature is summarized in Figure C.1.

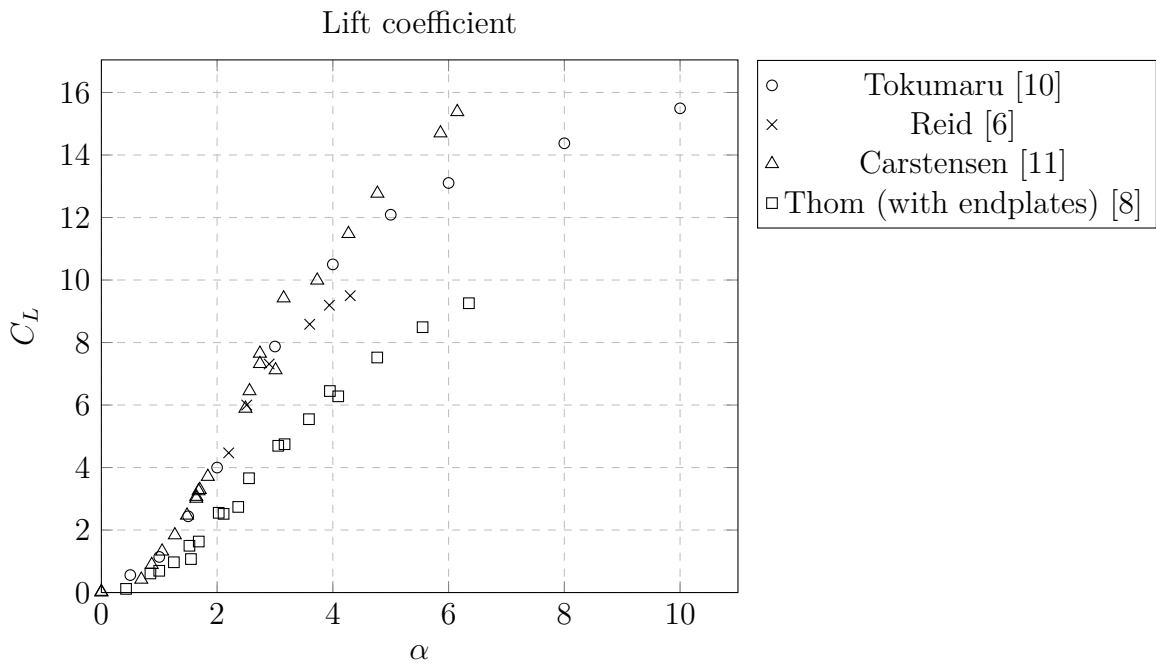


Figure C.1: Summary of experimental results for the lift coefficient.

Figure C.2 C_D as a function of the Reynolds number for a non-rotating cylinder. C_D for the 2D and 3D models are also plotted.

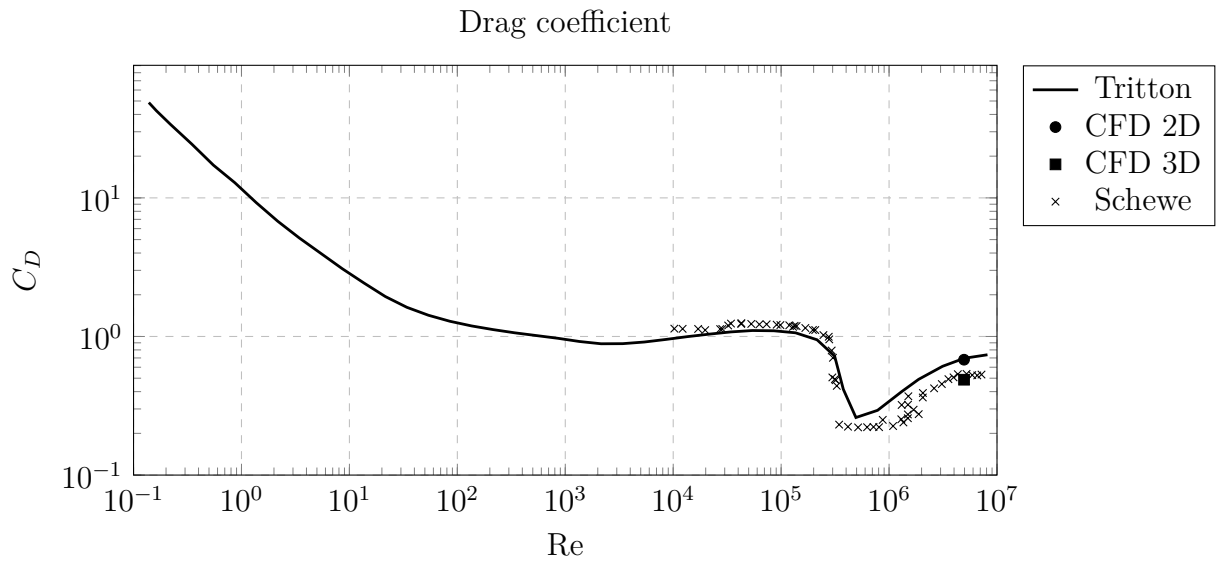


Figure C.2: Experimental results for C_D for a non-rotating cylinder as a function of Reynolds number, data from Tritton [33] and Schewe [32].

D

Appendix: 3D aspect ratio effects

Figure D.1 shows the difference in force and moment coefficients for aspect ratios of 6 and 10.

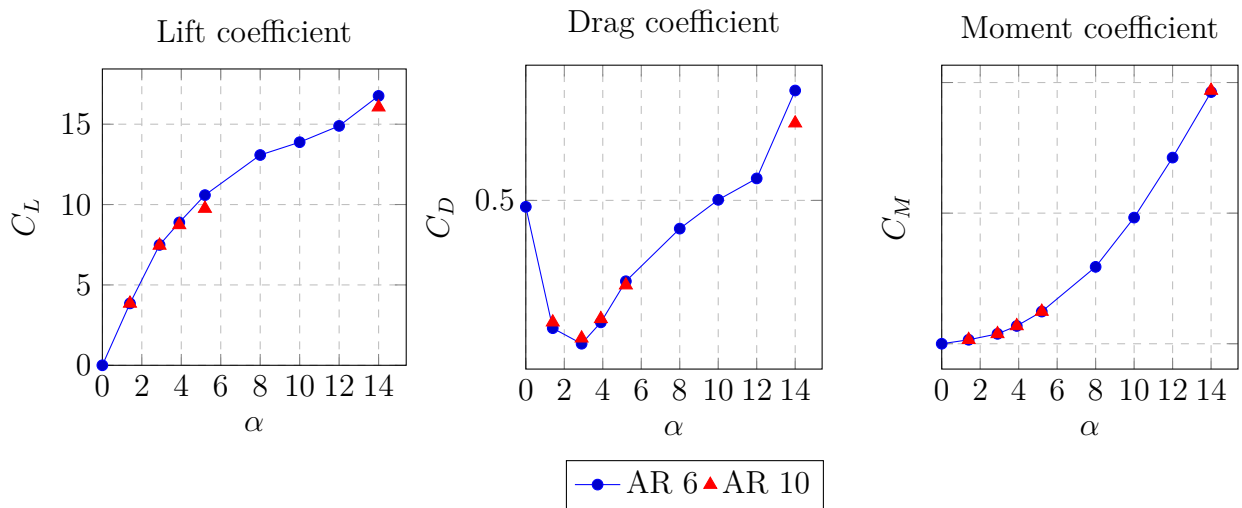


Figure D.1: Force and moment coefficient data as a function of speed ratio for different aspect ratios.

E

Appendix: 2D vortex shedding data

Table E.1 shows the magnitude and period of the coefficient oscillations for the 2D simulations.

Table E.1: Vortex shedding period, minimum, maximum and average coefficients for the 2D simulations. Steady forces are indicated with a dash.

α	0	1.4	2.9	3.9	5.2	6.0	8.0	10.0	12.0	14.0
Period	60 s	40 s	-	-	-	-	280 s	240 s	230 s	230 s
C_L , min	-0.59	3.72	-	-	-	-	19.04	19.35	19.15	18.93
C_L , max	0.57	3.90	-	-	-	-	20.17	21.25	20.75	22.21
C_L , avg	0.00	3.87	7.67	9.37	11.46	12.90	19.57	20.35	20.66	20.96
C_D , min	0.47	0.15	-	-	-	-	-0.42	-1.04	-2.13	-3.56
C_D , max	0.57	0.26	-	-	-	-	0.81	1.36	2.04	2.76
C_D , avg	0.64	0.16	0.10	0.10	0.09	0.08	0.17	0.14	-0.05	-0.13